HHS Public Access

Author manuscript

*Cell Rep*. Author manuscript; available in PMC 2024 February 05.

Published in final edited form as:

*Cell Rep*. 2023 November 28; 42(11): 113374. doi:10.1016/j.celrep.2023.113374.

# The expression profile and tumorigenic mechanisms of CD97 (ADGRE5) in glioblastoma render it a targetable vulnerability

**Niklas Ravn-Boess**[1], **Nainita Roy**[2], **Takamitsu Hattori**[3,4], **Devin Bready**[1], **Hayley Donaldson**[1], **Christopher Lawson**[1], **Cathryn Lapierre**[1], **Aryeh Korman**[5], **Tori Rodrick**[5], **Enze Liu**[6], **Joshua D. Frenster**[1], **Gabriele Stephan**[1], **Jordan Wilcox**[1], **Alexis D. Corrado**[3,4], **Julia Cai**[1], **Rebecca Ronnen**[1], **Shuai Wang**[1], **Sara Haddock**[1], **Jonathan Sabio Ortiz**[1], **Orin Mishkit**[7], **Alireza Khodadadi-Jamayran**[8], **Aris Tsirigos**[8], **David Fenyö**[4,9], **David Zagzag**[1,2], **Julia Drube**[10], **Carsten Hoffmann**[10], **Fabiana Perna**[11], **Drew R. Jones**[5], **Richard Possemato**[2,3], **Akiko Koide**[3,12], **Shohei Koide**[3,4], **Christopher Y. Park**[2,3], **Dimitris G. Placantonakis**[1,3,13,14,15,16,*]

[1]Department of Neurosurgery, NYU Grossman School of Medicine, New York, NY 10016, USA

[2]Department of Pathology, NYU Grossman School of Medicine, New York, NY 10016, USA

[3]Laura and Isaac Perlmutter Cancer Center, NYU Grossman School of Medicine, New York, NY 10016, USA

[4]Department of Biochemistry and Molecular Pharmacology, NYU Grossman School of Medicine, New York, NY 10016, USA

[5]Metabolomics Laboratory, NYU Grossman School of Medicine, New York, NY 10016, USA

[6]Department of Medicine, Division of Hematology/Oncology, Indiana University, Indianapolis, IN 46202, USA

[7]Preclinical Imaging Laboratory, NYU Grossman School of Medicine, New York, NY 10016, USA

[8]Applied Bioinformatics Laboratories, NYU Grossman School of Medicine, New York, NY 10016, USA

[9]Institute for Systems Genetics, NYU Grossman School of Medicine, New York, NY 10016, USA



*Correspondence: dimitris.placantonakis@nyulangone.org.

AUTHOR CONTRIBUTIONS

Conceived and designed the experiments, N.R.-B., N.R., T.H., D.R.J., R.P., A. Koide, S.K., C.Y.P., and D.G.P.; performed and aided with the experiments, N.R.-B., N.R., T.H., H.D., C. Lawson, C. Lapierre, A. Korman, T.R., J.D.F., G.S., J.W., A.D.C., J.C., R.R., S.W., S.H., J.S.O., O.M., D.Z., J.D., and C.H.; analyzed the data, N.R.-B., D.B., E.L., A.K.-J., A.T., D.F., F.P., and D.G.P.; wrote and edited the manuscript, N.R.-B. and D.G.P.

DECLARATION OF INTERESTS

S.K., T.H., A. Koide, C.Y.P., D.G.P., and the NYU Grossman School of Medicine have filed a patent application titled “Anti-CD97 antibodies and antibody-drug conjugates.” D.G.P. and the NYU Grossman School of Medicine own an EU and Hong Kong patent titled “Method for treating high-grade gliomas” on the use of GPR133 as a treatment target in glioma. D.G.P. has received consultant fees from Tocagen, Synaptive Medical, Monteris, Robeaute, Guidepoint, Servier Pharmaceuticals, and Advantis. S.K. was a scientific advisory board member and received consulting fees from Black Diamond Therapeutics; is a co-founder and holds equity in Aethon Therapeutics and Revalia Bio; and has received research funding from Aethon Therapeutics, Argenx BVBA, Black Diamond Therapeutics, and Puretech Health.

SUPPLEMENTAL INFORMATION

Supplemental information can be found online at https://doi.org/10.1016/j.celrep.2023.113374.

[10]Institute for Molecular Cell Biology, Universitätsklinikum Jena, 07745 Jena, Germany

[11]Moffitt Cancer Center, Tampa, FL 33612, USA

[12]Department of Medicine, NYU Grossman School of Medicine, New York, NY 10016, USA

[13]Kimmel Center for Stem Cell Biology, NYU Grossman School of Medicine, New York, NY 10016, USA

[14]Brain and Spine Tumor Center, NYU Grossman School of Medicine, New York, NY 10016, USA

[15]Neuroscience Institute, NYU Grossman School of Medicine, New York, NY 10016, USA

[16]Lead contact

## SUMMARY

Glioblastoma (GBM) is the most common and aggressive primary brain malignancy. Adhesion G protein-coupled receptors (aGPCRs) have attracted interest for their potential as treatment targets. Here, we show that CD97 (ADGRE5) is the most promising aGPCR target in GBM, by virtue of its *de novo* expression compared to healthy brain tissue. CD97 knockdown or knockout significantly reduces the tumor initiation capacity of patient-derived GBM cultures (PDGCs) *in vitro* and *in vivo*. We find that CD97 promotes glycolytic metabolism via the mitogen-activated protein kinase (MAPK) pathway, which depends on phosphorylation of its C terminus and recruitment of β-arrestin. We also demonstrate that THY1/CD90 is a likely CD97 ligand in GBM. Lastly, we show that an anti-CD97 antibody-drug conjugate selectively kills tumor cells *in vitro*. Our studies identify CD97 as a regulator of tumor metabolism, elucidate mechanisms of receptor activation and signaling, and provide strong scientific rationale for developing biologics to target it therapeutically in GBM.

## In brief

Ravn-Boess et al. show that CD97 serves as a promising target in GBM due to its *de novo* expression in GBM compared to healthy brain. They demonstrate that CD97 promotes Warburg-like metabolism through activation of the MAPK signaling cascade. Also, they target GBM cells using an antibody-drug conjugate against CD97.

## Graphical abstract

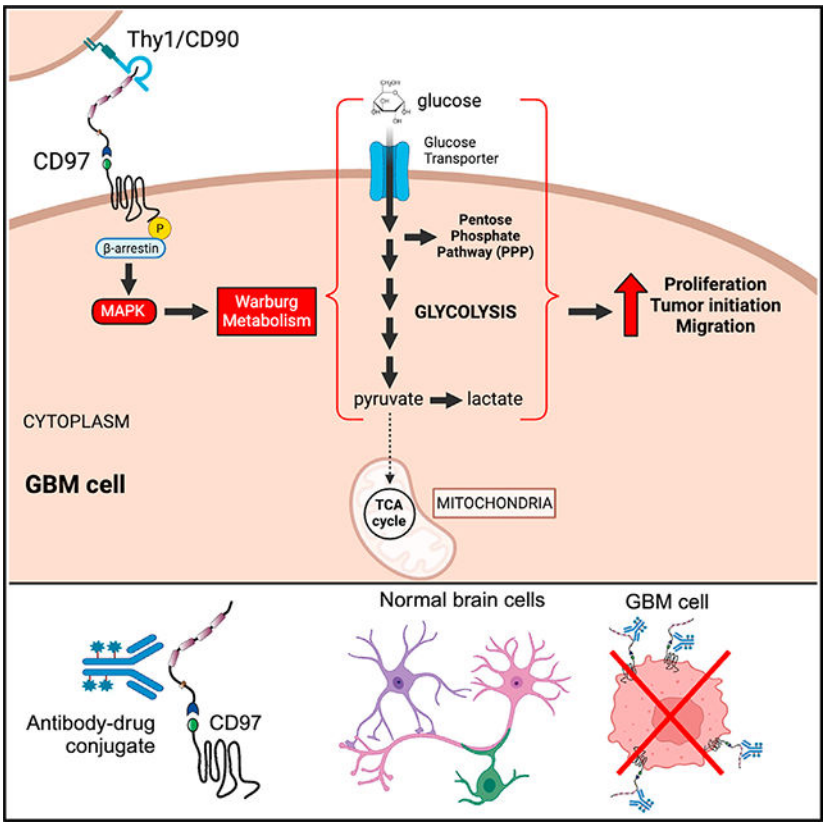


## INTRODUCTION

Glioma is the most common primary brain malignancy. In adults, two main types of glioma exist.[1,2] The less common type is typically encountered in younger patients and is driven by a neomorphic mutation in the metabolic enzyme isocitrate dehydrogenase (IDH). The more common type, also known as glioblastoma (GBM), is observed in older patients, lacks the IDH mutation (IDH-wild type or IDH-WT), has an aggressive course, and represents the largest unmet need in neuro-oncology. The current treatment regimen for GBM involves neurosurgical resection of the tumor followed by chemoradiotherapy. Nevertheless, these measures have done little to improve patient outcomes, with the median survival limited to about 15 months.[3–5] It is clear that in order to improve GBM treatment, we must identify new targetable vulnerabilities of tumor cells and their microenvironment.

In our effort to identify novel mechanisms contributing to GBM tumorigenesis, our group has become interested in the adhesion family of G protein-coupled receptors (aGPCRs), which consists of 32 members.[6] aGPCRs are characterized by large extracellular N termini that contain both receptor-specific domains determining ligand binding and a functionally conserved GPCR autoproteolysis-inducing (GAIN) domain, which catalyzes receptor cleavage at the GPCR proteolysis site (GPS).[7–9] Emerging evidence has implicated several aGPCRs in developmental, physiologic, and oncogenic processes.[6,10–15] This prompted us to compare the expression of all aGPCR members in cell types within healthy, non-neoplastic brain tissue; neural stem cells (NSCs), the putative cell of origin in GBM;[16–18]

and patient-derived GBM cultures (PDGCs). Our transcriptomic and proteomic expression analysis identified CD97 (ADGRE5) as the aGPCR with the largest differential expression profile: high expression in PDGCs derived from all transcriptional subtypes of GBM in The Cancer Genome Atlas (TCGA; proneural, classical, and mesenchymal)[2,19] and absence from healthy brain tissue and NSCs.

CD97 is expressed in several lineages of the immune system, where it is critical for the inflammatory response,[20–24] as well as in multiple liquid and solid malignancies.[13,25–28] Among these malignancies is GBM, in which CD97 was previously implicated in cellular proliferation, brain invasion, and tumor metabolism.[29–33] However, its mechanism of action in GBM remains incompletely understood. Furthermore, little research effort has been devoted to its therapeutic targeting. Here, we use PDGCs to demonstrate that CD97 is essential for tumor growth both *in vitro* and *in vivo*. Using transcriptomic, metabolomic, and signaling assays, we find that CD97 helps promote glycolytic metabolism via activation of the mitogen-activated protein kinase (MAPK) signaling pathway. We also identify THY1/CD90 as the most likely physiologically relevant CD97 ligand in GBM and demonstrate that CD97 signaling depends on phosphorylation of its C terminus and recruitment of β-arrestin. To capitalize on CD97's therapeutic potential, we show that a CD97 antibody-drug conjugate (ADC) that we have developed in-house specifically kills GBM cells, but not human astrocytes or NSCs, *in vitro*. Collectively, these data elucidate receptor activation and signaling mechanisms employed by CD97 to promote tumor growth and regulate tumor metabolism in GBM and highlight the receptor's potential as a therapeutically targetable vulnerability in GBM.

## RESULTS

### CD97 is *de novo* expressed in GBM relative to healthy brain

To compare the expression patterns of aGPCRs in GBM relative to healthy, non-neoplastic brain tissue, we undertook a combined transcriptomic and proteomic approach. First, we analyzed the mRNA expression levels of all 32 aGPCRs in healthy brain tissue using the Allen Brain Map database and in PDGCs collected in-house (Figure 1A). The transcriptional data suggested upregulated expression of several aGPCRs in GBM compared to healthy brain cell types. Second, we interrogated proteomic data from healthy brain[34] and GBM (CPTAC [Clinical Proteomic Tumor Analysis Consortium])[35] and confirmed *de novo* expression at the protein level for some aGPCRs (Figure 1B). Third, we compared the differential gene expression of aGPCRs between human NSCs, the putative cell of origin in GBM,[18] and PDGCs using bulk RNA sequencing (RNA-seq) data (Figures 1C and 1D). Collectively, we found that *CD97* fulfilled criteria for the single most differentially expressed aGPCR in GBM compared to healthy brain: it was one of the most upregulated aGPCRs in PDGCs and was detected in all 99 GBM specimens from the CPTAC database[35]; it was absent from non-neoplastic brain tissue at the transcriptomic and proteomic level; and the statistical significance of its transcriptional upregulation in PDGCs compared to NSCs was the highest genome-wide. To confirm these findings, we also performed immunofluorescent staining of healthy temporal lobe tissue sections and several (n = 5) GBM tissue sections and confirmed that CD97 was uniquely expressed in GBM and not in

healthy brain (Figure 1E). Confocal microscopy confirmed plasma membrane localization of the receptor in tumor cells within GBM biospecimens (Figure 1F). Using flow cytometry, we found robust surface expression of CD97 in all tested PDGCs (representing all three TCGA-defined transcriptional subtypes of GBM: proneural, classical, and mesenchymal[2,19]) and low expression in non-neoplastic human astrocytes (NHAs) and NSCs (Figures 1G and S1A). These data suggest that CD97 is *de novo* expressed in GBM relative to non-neoplastic brain tissue and that it is ubiquitously expressed in all GBM tumors.

We then tested whether *CD97* expression differs between IDH-wild-type (WT) GBM and low-grade IDH-mutant gliomas using single-cell RNA-/ATAC (assay for transposase-accessible chromatin)-seq data collected from an IDH-mutant WHO (World Health Organization) grade II astrocytoma and an IDH-WT GBM (Figure 1H). After identifying cell clusters based on single-cell RNA-seq gene expression (Figures 1I and S1B) via Seurat, we found that *CD97* expression was highest in IDH-WT GBM tumor cells and immune cells but substantially less abundant in IDH-mutant low-grade astrocytoma cells (Figure 1J). Analysis of single-cell ATAC-seq data using Signac demonstrated open, accessible chromatin at the *CD97* locus only in GBM and immune cell clusters but not in IDH-mutant astrocytoma cells and healthy brain lineages (Figure 1K). Similarly, chromatin immunoprecipitation (ChIP)-seq for H3K27 acetylation, an activating chromatin modification, obtained from publicly available Gene Expression Omnibus (GEO) datasets,[36] showed increased activation around the *CD97* promoter in IDH-WT GBM but not in IDH-mutant gliomas (Figure 1L). Together, these findings suggest that CD97 expression is abundant in IDH-WT GBM but only limited in low-grade IDH-mutant astrocytoma.

Alternative splicing of *CD97* mRNA generates three distinct isoforms that differ in the number of epidermal growth factor (EGF)-like repeats in the N-terminal extracellular domain (ECD) of the receptor (Figure 1M).[25] Analysis of TCGA RNA-seq data indicated that isoforms 2 and 3 were the predominant variants in GBM (Figure 1N). The *CD97* transcript was found in all transcriptional subtypes of GBM in TCGA (Figure S1C). The extent of autoproteolytic cleavage for each aGPCR sometimes varies depending on the cellular context and cell type.[37] To test whether CD97 undergoes cleavage at the GPS in GBM, we exogenously expressed all three isoforms of CD97 and a non-cleavable point mutant of CD97 (CD97 S531A)[38] in PDGCs (Figure 1O). Immunoblotting against the ECD and the intracellular domain (ICD) of CD97 revealed that the vast majority of the receptor undergoes cleavage in PDGCs to generate a membrane-bound C-terminal fragment (CTF) and an extracellular N-terminal fragment (NTF), regardless of the isoform that is overexpressed (Figure 1P). To resolve discrepancies in the expected and observed molecular weights of the NTF (Figure S1D), we deglycosylated whole-cell lysates collected from a PDGC endogenously expressing CD97 or exogenously overexpressing the CD97 isoforms before immunoblot staining. The deglycosylation resulted in band shifts to the expected molecular weights (Figure S1E), suggesting that the CD97 NTF is glycosylated. Interestingly, the band corresponding to the endogenously expressed deglycosylated CD97 NTF appears to match the molecular weight of the NTF of the exogenously expressed shorter CD97 isoforms (Figure S1E). This finding supported the transcriptomic TCGA data indicating that the predominant species of CD97 in GBM are the shorter isoforms (with

three or four extracellular EGF repeats) and suggested that CD97 undergoes autoproteolytic cleavage in GBM.

## CD97 loss compromises GBM growth

To further investigate the role of CD97 in GBM, we established short hairpin RNAs (shRNAs) and guide RNAs (gRNAs) targeting all isoforms of CD97 (Figures 2A and S2A). Flow cytometric surface staining confirmed loss of CD97 upon shRNA-mediated knockdown (Figure 2B) and CRISPR-Cas9-mediated knockout (Figure S2B). Since CD97 is implicated in GBM cell migration,[29,32,33] we performed a Transwell migration assay that confirmed significant reduction in PDGC migration after lentiviral infection with the CD97 shRNA compared to a scrambled (SCR) shRNA control (Figure S2C). Importantly, knockdown of CD97 produced a substantial growth defect in our PDGCs *in vitro*. This was quantified using tumorsphere formation assays, which revealed a significant loss of tumorsphere formation after CD97 knockdown (Figures 2C and 2D). Overexpression of a doxycycline (dox)-inducible shRNA-resistant form of *CD97* cDNA alone did not increase tumorsphere formation in PDGCs (Figure S2D) but did rescue the impairment in tumorsphere formation following CD97 knockdown (Figures 2C and 2D), suggesting specificity of the phenotype observed with CD97 shRNA. The effects of CD97 knockdown on PDGCs were also observed in extreme limiting dilution assays (ELDA) (Figures 2E and 2F), suggesting a diminished clonogenic frequency and impaired GBM stem cell self-renewal in the absence of CD97. We also observed significant effects of CD97 on cellular proliferation using cell-cycle analysis (Figure S2E) and Ki67 immunofluorescent staining (Figure S2F), as well as on cellular viability using flow cytometry for Annexin-V and DAPI (4′,6-diamidino-2-phenylindole) staining (Figure S2G). In contrast, CD97 knockdown in NHAs did not compromise their proliferation or their viability (Figures S2E and S2G). CRISPR-Cas9 knockout of CD97 phenocopied the shRNA knockdown and significantly hindered PDGC growth and viability relative to a gRNA directed at the safe harbor human *ROSA26* locus in a cell competition assay (Figure 2G). To determine whether CD97 knockdown also impaired tumor formation *in vivo*, intracranial xenograft assays were performed in immunodeficient NSG mice. Implantation with PDGCs following CD97 knockdown resulted in significantly less tumor growth (Figures 2H–2J) and significantly prolonged mouse survival (Figure 2K). These findings demonstrate that CD97 loss compromises PDGC proliferation and viability and reduces tumor initiation *in vitro* and *in vivo*.

## CD97 knockdown impairs glycolytic metabolism

To elucidate mechanisms underlying the actions of CD97 in PDGCs, bulk RNA-seq was performed following knockdown of the receptor in one of our PDGCs. In order to capture early consequences of CD97 knockdown before any effects on cellular viability, we collected cells 4 days after infection with the lentiviral shRNA vector. Over 3,000 genes were differentially expressed between the CD97 knockdown and the SCR shRNA control PDGCs (Figure 3A). Among the most downregulated genes was *CD97*, confirming a robust knockdown of the receptor (Figure 3A). Gene Ontology (GO) PANTHER pathway analysis was used to detect gene sets that were enriched and depleted upon CD97 knockdown. Interestingly, aerobic respiration was the most enriched pathway, while

glycolytic metabolism was identified as the most depleted biological process (Figure 3B). This was noteworthy because GBM tumor cells exhibit increased reliance on glycolytic metabolism, a phenomenon known as the Warburg effect, compared to healthy brain cells.[39–42] This led us to hypothesize that CD97 plays a role in promoting glycolysis in GBM.

Indeed, when we revisited the differential gene expression data, we found that the majority of genes involved in glycolysis and glucose transport were downregulated upon CD97 knockdown, while the opposite was observed for genes involved in the tricarboxylic acid (TCA) cycle and in oxidative phosphorylation (OXPHOS) (Figure 3A). In order to further visualize this, we performed a differential gene correlation analysis (DGCA) of our transcriptomic data from a PDGC following both overexpression and knockdown of CD97 (Figure 3C). This analysis also revealed that *CD97* expression levels positively correlated with many genes relevant to glycolysis and negatively correlated with genes relevant to the TCA cycle (Figure 3C). We also confirmed a reduction in the glucose transporter GLUT3 (*SLC2A3*) after CD97 knockdown at the protein level via immunoblot staining (Figure S3A). Of note, several glycolytic enzymes and glucose transporters have been previously implicated in GBM pathogenesis[42–45] and metabolic reprogramming.[46–48] In order to ensure that the effects of CD97 knockdown on the transcription of metabolic genes were generalizable, we performed gene set enrichment analysis (GSEA) on RNA-seq data collected from three other PDGCs following CD97 knockdown. Here, we also observed a depletion of glycolytic processes and an enrichment of OXPHOS-related transcripts following CD97 knockdown (Figures S3B–S3D).

Based on the transcriptomic data, we decided to investigate the metabolic consequences of CD97 perturbation in our PDGCs. Since Warburg metabolism is characterized by glucose catabolism biased toward lactate generation rather than pyruvate conversion to acetyl-CoA for utilization in the TCA cycle, we measured lactate levels in the culture medium after shRNA-mediated silencing or overexpression of CD97 in our PDGCs (Figure 3D). Indeed, CD97 knockdown resulted in reduced levels of extracellular lactate, while levels increased upon CD97 overexpression. We next performed both steady-state metabolomics and glucose tracing analysis in order to gain further insight on the regulation of enzymatic steps of glucose metabolism. Steady-state metabolomic data showed a depletion of glycolytic metabolites following CD97 knockdown (Figure 3E). Given that glycolytic intermediates feed into both the TCA cycle and the pentose-phosphate pathway (PPP), which is essential for nucleic acid synthesis and redox homeostasis, it is no surprise that these metabolites were also depleted after CD97 knockdown (Figures 3E and S3E).[49] Glucose tracing data generated using [U-$^{13}C_6$]-glucose also revealed reduced levels of heavy carbon incorporation into glycolytic metabolites, including pyruvate, while the effects on TCA cycle metabolites were less evident (Figures 3F and S3F). Consistent with these findings, we found that exogenous pyruvate rescued PDGC tumorsphere formation following CD97 knockdown (Figure S3G). Collectively, the transcriptomic and metabolomic data suggest that CD97 knockdown leads to a global reduction in glucose catabolism, which is likely to account for the reduced proliferation and viability of GBM cells. We postulate that the upregulation of transcripts encoding enzymes of the TCA cycle and OXPHOS reflects inadequate compensation aimed to meet energy demands impacted by reduced glycolysis.

To further test the hypothesis that CD97 promotes glycolytic metabolism at a functional level, we measured rates of glycolysis and mitochondrial respiration using a Seahorse XF Cell Energy Phenotype assay. This assay measures the extracellular acidification rate (ECAR), largely accounted for by lactate production, and the oxygen consumption rate (OCR) before and after the addition of mitochondrial stressors (oligomycin and FCCP). PDGCs following CD97 knockdown exhibited a loss of the ability to respond to mitochondrial stressors (Figure 3G). Closer investigation revealed a significantly decreased ECAR both at baseline and after the addition of mitochondrial stressors (maximal ECAR) (Figures 3H and 3I). Though the OCR levels were also decreased following CD97 knockdown, these effects were not as striking as those with ECAR and did not reach statistical significance at baseline (Figures 3J and 3K). Together, these data suggest that CD97 promotes glycolytic metabolism in GBM.

## CD97 activates the MAPK/ERK signaling pathway

In an effort to identify signaling pathways activated by CD97 in GBM, we revisited the GO PANTHER pathway analysis of our RNA-seq data shown previously (Figure 3B). Here, transcripts involved in the ERK1/ERK2 signaling cascade were depleted upon CD97 knockdown in our PDGCs. To confirm whether the MAPK pathway is activated by CD97 in our PDGCs, we performed immunoblot staining against phosphorylated ERK1/ERK2 following CD97 knockdown or overexpression. CD97 knockdown significantly decreased levels of phosphorylated ERK1/ERK2 (Figure 4A). In contrast, overexpression of all CD97 isoforms led to significant increases in phosphorylated ERK1/ERK2 in most of our PDGCs (Figure 4B). These results suggested that CD97 activates the MAPK signaling pathway.

To test whether activation of the MAPK signaling pathway rescues the metabolic and growth phenotypes observed after CD97 knockdown, we stably transfected PDGCs with a phosphomimetic MEK mutant (MEK S218D,S222D; denoted as $MEK^{DD}$ onward), which is expected to constitutively phosphorylate and activate ERK1/ERK2.[50] We confirmed that the $MEK^{DD}$ mutant increased ERK1/ERK2 activation by performing an immunoblot against phosphorylated ERK (Figure S4A). Transfection of PDGCs with the $MEK^{DD}$ mutant restored lactate levels (Figures 4C and 4D) and their overall metabolic profile in Seahorse Cell Energy Phenotype assays following CD97 knockdown (Figure 4E). Of particular interest was the finding that $MEK^{DD}$ rescued the CD97 knockdown-imparted defect in the ECAR, but not in the OCR (Figure 4F), suggesting that the CD97-MAPK signaling axis not only promotes glycolysis but also biases conversion of pyruvate to lactate rather than to acetyl-CoA. Equally importantly, the $MEK^{DD}$ construct also rescued tumorsphere formation after knockdown of CD97 in PDGCs (Figures 4G and 4H). Together, these data suggest that CD97 activates MAPK signaling to promote glycolytic metabolism, thus enabling tumor growth in GBM.

## CD97 activates the MAPK signaling cascade through phosphorylation of its C terminus and recruitment of β-arrestin

In addition to the MAPK signaling pathway, past research on CD97 has identified other signaling mechanisms, including G protein-mediated $G\alpha_i$ (reduces cyclic-AMP) and $G\alpha_{12/13}$ (activates RHOA) activation and PI3K/AKT pathway activation (Figure

5A).[27,31,51,52] We investigated whether CD97 influenced these other signaling pathways in our PDGCs. CD97 overexpression in our PDGCs did not alter canonical G protein-mediated signaling as measured by luciferase reporter assays (Figure S4B). In addition, CD97 overexpression did not alter $G\alpha_{12/13}$-mediated activation of RHOA in pull-down assays specific to GTP-bound RHOA (Figure S4C). Finally, phosphorylation of AKT was unchanged by perturbations in CD97 levels (Figure S4D). This led us to explore alternative GPCR signaling mechanisms.

Many GPCRs are phosphorylated by GPCR kinases (GRKs), a modification that leads to recruitment of β-arrestin.[53] β-Arrestin acts as a scaffold, enabling recruitment of components of the MAPK pathway to GPCRs, thereby facilitating subsequent activation of this signaling pathway,[54,55] in addition to its well-described roles in GPCR desensitization and internalization.[56] To determine whether CD97 undergoes phosphorylation in GBM, we analyzed phosphoproteomic data from GBM in the CPTAC database.[35] Indeed, we identified five serine/threonine phosphorylation sites within the cytosolic C terminus of CD97 (Figure 5B). Three of these phosphorylation sites (T816, S818, and T820) were found in the vast majority of the GBM samples tested and also demonstrated a strong positive correlation in their abundance to one another (Figures S4E and S4F). This finding prompted us to test whether CD97 phosphorylation recruits β-arrestin as a potential mechanism for MAPK pathway activation. We generated a CD97 isoform 3 truncation mutant (denoted as ΔPS CD97 onward) lacking amino acids 762–784, which include the five aforementioned and one previously described[52] phosphorylated residues (Figure S4G). We verified localization of the ΔPS CD97 mutant to the cell membrane via immunofluorescent staining of the CD97 N terminus after construct overexpression in HEK293 cells (Figure S4H). When we performed a fluorescence resonance energy transfer (FRET)-based β-arrestin recruitment assay in GBM cells, we observed an enhanced signal upon WT CD97 overexpression, an effect that was no longer observed after overexpression of the ΔPS CD97 construct (Figure 5C). Furthermore, overexpression of the ΔPS CD97 mutant was not able to induce phosphorylation of ERK1/ERK2 (Figures 5D and 5E) and failed to rescue tumorsphere formation in PDGCs following CD97 knockdown, as measured by a tumorsphere formation assay (Figure 5F). To test whether this mechanism was dependent on GRK phosphorylation of the CD97 C terminus, we first determined which GRK isoforms had the highest expression in our PDGCs (Figure S4I). We identified *GRK2* and *GRK6* as the most highly expressed members of the GRK family in GBM. Using transgenic HEK293 cells harboring CRISPR-Cas9 knockouts of GRK2, GRK6, or both,[53] we found that both GRK2 and -6 contribute to CD97-mediated activation of ERK1/2 (Figures S4J and S4K). These data suggest that the CD97-MAPK signaling axis requires phosphorylation of the cytosolic C terminus of CD97 by GRK2/6 and recruitment of β-arrestin.

## THY1/CD90 is the most likely CD97 ligand in GBM

CD97 is known to interact with several ligands, including CD55, a glycosylphosphatidylinositol (GPI)-linked membrane-tethered protein that regulates the complement cascade in immune cells, and THY1/CD90, another GPI-linked protein found on neurons, immune cells, and activated endothelium.[57–59] To gain insight into the expression profile of putative CD97 ligands in GBM, we investigated our own, as well

as publicly available single-cell RNA-seq data in GBM (Figures 5G–5I and S5A–S5F).[59,60] While *CD55* expression was largely confined to immune cells, *THY1/CD90* was found in tumor cells, as well as non-neoplastic brain cell lineages (Figures 5G–5I). That *THY1/CD90* is abundantly expressed in GBM cells, as well as in neurons, was corroborated by our initial investigation of transcript levels in our PDGCs and brain cell types (Figure 1A). Furthermore, surface staining of PDGCs for CD55 and THY1/CD90 in flow cytometry assays revealed varied expression of CD55 but consistently high levels of THY1/CD90 (Figure 5J).

Based on these findings, we then tested whether we could further enhance CD97-activated MAPK signaling in PDGCs by exposure to recombinant forms of CD55 and THY1/CD90. We found that plating CD97-overexpressing PDGCs on wells coated with recombinant THY1/CD90 resulted in increased levels of phosphorylated ERK1/ERK2 (Figure 5K), an effect that was not observed to the same extent in cells transduced with an empty vector (EV) control (Figure 5L). Though CD55 also led to some increases in phosphorylated ERK1/ERK2, the effect was limited and did not reach statistical significance. Collectively, these data suggest that THY1/CD90 is the most likely activating ligand of CD97 in GBM.

### A CD97-targeting ADC selectively kills PDGCs but not astrocytes or NSCs

Since CD97 exhibits high expression in GBM and is absent from healthy brain tissue, we tested whether CD97 could be targeted therapeutically. We generated a human CD97-specific antibody by performing *in vitro* selection of a human synthetic antibody library (Figure 6A). We found that the anti-CD97 antibody exhibited significantly increased internalization into PDGCs when compared to an immunoglobulin G1 (IgG1) LALA isotype control that does not bind to any known target (Figure S6A). We then conjugated this antibody to monomethyl auristatin F (MMAF), a membrane-impermeant anti-tubulin agent blocking cytoskeletal polymerization and thereby cytotoxic to dividing cells,[61] to generate an anti-CD97 ADC. We observed a lower lethal dose ($LD_{50}$) in patient-derived and U87 GBM cells compared to control cells (NHAs, NSCs, and HEK293 cells) in WST8 viability assays (Figures 6B, 6C, and S6B–S6E). Since the WST8 reagent relies on the presence of cellular metabolites, the assay's range depends on the metabolic activity of the cells, which varies considerably among PDGCs, NSCs, and relatively non-proliferative NHAs. Therefore, we also stained cells with Hoechst 33342 dye after treatment and took representative images to obtain cell counts (Figures 6D and 6E). From these images, the specificity of the CD97 ADC was even more evident, as GBM cells decreased in number, while NSC and NHA numbers remained stable. Together, these findings suggest that the *de novo* expression of CD97 in GBM relative to healthy brain can be exploited therapeutically through the use of ADCs (Figure 6F).

## DISCUSSION

GBM tumors resist multimodal treatment regimens, all but guaranteeing disease recurrence in patients. Identifying new targets for GBM is essential for ameliorating therapy, an already difficult task given GBM's extensive intertumoral and intratumoral heterogeneity.[2–5,19] aGPCRs are an understudied group of transmembrane receptors with emerging roles in

oncology[10–12] that show promise as therapeutic targets.[6–9] Our group previously identified the aGPCR GPR133 (ADGRD1) (Figure 1A) as an essentiality in GBM.[11,62] Here, we demonstrate that another member of the aGPCR family, CD97 (ADGRE5), is ubiquitously expressed and significantly more abundant than GPR133 in GBM, regardless of TCGA transcriptional subtype, thereby overcoming issues of intertumoral heterogeneity. Equally importantly, CD97 is absent from healthy non-neoplastic brain tissue, further increasing its potential as a therapeutic target for GBM. In fact, the transcriptional upregulation of *CD97* mRNA in GBM relative to NSCs, the putative cell of origin in glioma, is associated with the highest statistical significance genome-wide (Figure 1). Consistent with this expression profile, PDGCs treated with our in-house-generated CD97 ADC demonstrated a significantly greater cell death than human astrocytes and NSCs, which lack CD97 expression (Figure 6). Collectively, our data suggest that CD97 in GBM is, by virtue of its expression profile, the most appealing treatment target among the aGPCRs and possibly one of the most targetable cell surface proteins genome wide. Furthermore, its essential tumorigenic functions in GBM suggest not only that therapeutic targeting can be accomplished via ADC platforms but also that neutralizing antibodies may also be beneficial. A crucial next step in investigating the therapeutic benefits of our CD97 ADC would be to treat orthotopic tumor xenografts *in vivo* with the ADC compound. The treatment schedule and dosage, along with the method of drug administration, whether it be systemic or intracranial/intratumoral, would require optimization. The endogenous expression of CD97 by immune cells and other extracranial tissues warrants concern for peripheral toxicity if the ADC were to be administered systemically in patients. CD97 neutralization with a systemically administered monoclonal antibody, for example, has been found to reduce granulocyte infiltration to sites of inflammation and relieve arthritic activity in mice,[24] corroborating our concern for possible extracranial toxicity of systemically administered CD97 biologics. In order to avoid targeting immune cells or other CD97-expressing tissues, delivery of antibody therapy within the tumor or the brain may be preferred. Novel approaches are being developed to carry out such localized treatments.[63] Future studies would also be needed in order to test the impact of this CD97-targeting ADC on other CD97-expressing malignancies.

Historically, CD97 was first discovered as a leukocyte receptor and characterized in the context of the immune system.[20–22,56] Since then, however, CD97 has been implicated in multiple malignancies, including hematologic (leukemia) and solid (esophageal, stomach, colorectal, hepatocellular, pancreatic, thyroid, prostate, ovarian, breast) tumors.[25–28] CD97 expression in GBM was first demonstrated in 2012, when it was found to confer a migratory phenotype.[33] More recent work has also implicated CD97 in cellular proliferation, GBM stem cell self-renewal, and tumor metabolism,[29–32] but the underlying mechanisms have not been elucidated. Here, we have taken a methodical approach to characterize the oncogenic function of CD97 in GBM using PDGCs from all TCGA-defined transcriptional subtypes (proneural, classical, mesenchymal) and advanced genetic, transcriptomic, metabolomic, cellular, and biochemical approaches. Our detailed study not only describes phenotypic contributions of CD97 to cellular proliferation, tumor initiation, GBM stem cell self-renewal, metabolism, and migration but also presents detailed molecular mechanisms accounting for these phenotypes.

Tumor metabolism, which relies both on the availability of nutrients and their utilization by tumor cells, is a critical determinant of oncogenesis at the interface of tumor cell-intrinsic biology and the microenvironment. GBM, like many other malignancies, manifests a dependency on glycolytic metabolism rather than on TCA cycle and OXPHOS. The predilection for glycolysis, which occurs in both normoxic conditions and in the severely hypoxic niches of GBM, is known as Warburg metabolism.[39–41,64] This metabolic adaptation is thought to allow generation of sufficient consumable energy in the form of ATP but also enables carbon skeleton conservation that is essential for biomass generation in enlarging tumors.[65] The mechanisms that regulate GBM's dependency on glycolysis remain incompletely understood. Our data suggest an important role for CD97 in the regulation of GBM cellular metabolism, and glycolysis in particular. *CD97* mRNA transcript levels show a striking positive correlation with transcripts encoding most glycolytic enzymes and a negative correlation with the expression of most TCA cycle enzymes. Using steady-state metabolomics, we found that CD97 knockdown resulted in a profound depletion of the majority of glycolytic metabolites, as well as metabolites within the TCA cycle. Since glycolytic products feed into TCA cycle and mitochondrial metabolism via the conversion of pyruvate to acetyl-CoA, it is not surprising that reduced levels of glycolytic metabolites result in reduced levels of TCA cycle intermediates. Mechanistically, we theorize that CD97 signaling promotes transcription of glycolytic transcripts, including *LDHA* (lactate dehydrogenase A) (Figure 3C), which catalyzes conversion of pyruvate to lactate at the expense of the pyruvate to acetyl-CoA reaction that feeds into the TCA cycle. We postulate that the upregulation of certain TCA cycle and OXPHOS transcripts upon CD97 knockdown signifies a compensatory, but ultimately inadequate, adaptation by cells in order to increase ATP production and meet cellular energy needs. More investigation is needed to determine the full mechanism whereby CD97 is impacting rates of glycolysis beyond effects on transcription rates of relevant genes.

The synthesis of our experimental data led us to formulate the hypothesis that CD97's effects on GBM cellular metabolism and tumor growth are driven by its activation of the MAPK/ERK pathway.[31,51] This pathway has been implicated in a slew of cellular functions, including cellular metabolism, proliferation, and migration.[66] From the metabolism point of view, MAPK signaling modulates several enzymes involved in glycolytic and TCA cycle/OXPHOS pathways.[45,67,68] Mutations that lead to overactivation of the MAPK pathway, such as in *RAS* or *RAF*, are often observed in malignancies and have been linked to their metabolic reliance on glycolysis and the PPP.[49,69] Pancreatic tumors driven by the oncogenic KRAS G12D mutation, for example, exhibit overactivation of the MAPK pathway, leading to redirection of glycolytic intermediates into the PPP and overall metabolic reprogramming.[49] Determining the exact mechanism by which CD97-activated MAPK signaling influences cell metabolism and other cell functions is a crucial next step of investigation prompted by this study. For example, whether CD97-MAPK signaling leads to post-translational modifications, such as phosphorylation, of relevant metabolic enzymes remains to be seen.

The impact of CD97 on GBM biology mirrors some of its actions in physiological processes. Within the immune system, CD97 has been shown to be critical for the inflammatory response by mediating cellular adhesion and migration.[20–22,56] For example,

CD97-expressing immune cells have been shown to bind to THY1/CD90-expressing activated endothelial cells,[59] which may represent an important step in leukocyte recruitment and diapedesis at inflamed tissues. Our demonstration of CD97-mediated regulation of cellular metabolism does not necessarily exclude these previously established functions in inflammation and cellular migration. In fact, it is well-documented that inflammation induces a metabolic shift in immune cells, leading to a greater reliance on glycolysis.[70] Furthermore, CD97 is expressed in macrophages, neutrophils, and T cells and is upregulated upon their activation during the immune response, an event accompanied by an increased metabolic reliance on glycolysis.[20,21,48,56,71–74] The link between metabolism and cell motility is thoroughly documented, but their interplay remains complex.[75–78] Migratory cells, for example, have been shown to increase glucose uptake by upregulating expression of glucose transporters. This enables localized bursts in glycolysis at sites undergoing cellular contraction needed for cell motility.[75,77] In this way, CD97's role in cellular metabolism may complement its previously established role in cellular migration. It is likely that CD97 plays similar functions in activated immune cells and in cancer cells, both of which share predilections for glycolytic metabolism and exhibit extended capacities of migration and proliferation.

Past studies on CD97 have suggested dependencies on multiple signaling mechanisms. A study in prostate cancer cells found that CD97 coupled with $G\alpha_{12/13}$, ultimately activating the RHOA pathway and promoting cellular migration.[27] Another study in human retinal pigment epithelium found that overexpression of CD97 activates MAPK signaling, as measured by increased serum response element (SRE)-driven luciferase expression in a luciferase reporter system.[79] Interestingly, we did not observe this finding using an SRE-driven luciferase assay in our PDGCs, nor did we detect any other G protein coupling of CD97 in GBM cells using other luciferase-driven reporter systems (Figure S4B). We previously found that CD97 activated both MAPK and AKT signaling in leukemic stem cells.[26] In our PDGCs, we only observed increased levels of phosphorylated ERK1/ERK2 but not phosphorylated AKT (Figure S4D). A study in colorectal cancer cells demonstrated that CD97 underwent phosphorylation at its C terminus, which ultimately regulated proper cytoskeletal organization and adhesion.[52] In a different study, GRK6 was shown to phosphorylate CD97, leading to receptor internalization.[80] Our analysis of phosphoproteomic data from GBM biospecimens identified robust phosphorylation of serine/threonine residues at the cytosolic C terminus of CD97, a finding that prompted us to investigate the involvement of β-arrestin in CD97-MAPK signaling. β-Arrestin is known to act as a scaffold for MAPK components, thereby facilitating pathway activation.[54] Indeed, we showed β-arrestin recruitment to the phosphorylated C terminus of CD97. In order to test the role of the phosphorylated C terminus in CD97 signaling, we generated a ΔPS CD97 mutant lacking the phosphorylated serine/threonine residues and found that the truncation abolished β-arrestin recruitment and MAPK activation. A limitation of this experimental approach is that removal of the C terminus may compromise other aspects of CD97 function, such as G protein coupling, that our assays have failed to detect, or receptor internalization, which may confound interpretation of this result. In the future, we will consider performing site-directed mutagenesis to interrogate each one of the phosphorylated serine/threonine residues individually in relation to CD97 signaling and function in GBM.

Another important aspect of our study is the characterization of CD97-ligand interactions of relevance in GBM. CD97 has a number of known extracellular ligands and binding partners, including the GPI-linked proteins CD55 and THY1/CD90.[59,60] In contrast to CD55, THY1/CD90, a known neuronal marker, exhibited abundant expression in GBM cells (Figures 1A, 1B, 5I, 5J, and S5D). When CD97-overexpressing PDGCs were plated on recombinant THY1/CD90, we observed a significantly more pronounced increase in MAPK signaling relative to plating on CD55 (Figures 5K and 5L). Together, these data suggest that CD97-activated MAPK signaling most likely relies on the activating ligand THY1/CD90.[58] Previous studies have implicated THY1/CD90 in GBM pathogenesis and other malignancies.[81,82] THY1/CD90 is known to form complexes with integrins, which have also been described as CD97 binding partners.[83] Further insight into the binding interaction between CD97, THY1/CD90, and other putative ligands would help elucidate how crucial this binding is to the phosphorylation of the CD97 C terminus, the recruitment of β-arrestin, and the activation of the MAPK signaling pathway. Additionally, the impact of autoproteolytic cleavage, which we observed for both endogenous and exogenous CD97 in PDGCs, on CD97 signaling is a future research aim.

Gliomas are broadly categorized based on their expression of a neomorphic mutation in the IDH enzyme.[5] WT IDH is found in both the cytoplasm and the mitochondria, where it catalyzes the decarboxylation of isocitrate to α-ketoglutarate (α-KG). The mutant form of IDH, however, generates the oncometabolite 2-hydroxyglutarate (2-HG). In response to 2-HG accumulation, IDH-mutant cells increase levels of OXPHOS and reduce lactate production by silencing *LDHA* expression.[84,85] This metabolic reprogramming in IDH-mutant glioma lies in stark contrast to that which occurs in IDH-WT GBM, where cells are characterized by increased Warburg metabolism. Our single-cell multiomic and ChIP-seq analyses found that *CD97* gene expression is robust in IDH-WT GBM but significantly lower in low-grade IDH-mutant glioma (Figure 1I). This finding correlates with the metabolic profiles of the two glioma types and is consistent with our hypothesis that CD97 promotes Warburg metabolism.

In summary, our study identifies CD97 as the aGPCR with the widest differential expression pattern in IDH-WT GBM vs. healthy brain tissue and NSCs, the putative cell of origin. We also show that CD97 functions to promote Warburg metabolism via a signaling mechanism that includes phosphorylation of the receptor's cytosolic C terminus, recruitment of β-arrestin, and activation of MAPK signaling. Finally, we use a CD97-ADC to selectively target GBM cells. Overall, these studies reveal insights regarding the role of CD97 in GBM, suggesting that CD97 represents an appealing therapeutic vulnerability in GBM and that its targeting will be impactful in future clinical trials.

## Limitations of the study

Our study describes the *de novo* expression of CD97 in GBM relative to non-neoplastic brain tissue and neural progenitors but does not dissect epigenetic and transcription factor-dependent mechanisms underlying this transcriptional profile. Phenotypically, our work has identified a robust effect of CD97 signaling on transcriptional regulation of gene networks encoding enzymes relevant to glycolytic metabolism, but it remains unclear whether it also

influences enzymatic function directly at specific nodes of the glycolytic pathway. While our data suggest that the CD97/CD90 interaction may be the most relevant to CD97 activation in GBM, we have not obtained biochemical validation of this interaction in GBM, nor have we tested mechanisms underlying its impact on CD97 receptor activation. In addition, our search for relevant CD97 ligands focused on the previously known interactors CD55 and CD90 but did not include unbiased discovery platforms for alternative ligand identification. Finally, our implementation of anti-CD97 ADC in GBM therapy will have to be tested in preclinical xenograft models *in vivo*.

## STAR★METHODS

### RESOURCE AVAILABILITY

**Lead contact—**Further information and requests for resources and reagents should be directed to and will be fulfilled by the lead contact, Dimitris Placantonakis (dimitris.placantonakis@nyulangone.org).

**Materials availability—**Expression plasmids and cell lines generated in this study (detailed in the key resource table) will be available upon request.

#### Data and code availability

- Transcriptomic data and multiomic data generated by this study have been deposited in the Gene Expression Omnibus (GEO) and are publicly available under the identifiers GSE230389 and GSE230393.
- This paper does not report original code.
- Any additional information required to reanalyze the data reported in this paper is available from the lead contact upon request.

### EXPERIMENTAL MODEL AND SUBJECT PARTICIPANT DETAILS

**Cell culture—**PDGCs were established and maintained.[11,37,89] In brief, fresh operative specimens were obtained from patients undergoing surgery for resection of GBM after informed consent (NYU IRB study 12–01130). Specimens were mechanically minced using surgical blades followed by enzymatic dissociation using Accutase (Cat# AT104, Innovative Cell Technologies). Cells were either long-term maintained in spheroid suspension cultures (tumorspheres) on untreated cell culture dishes or grown as attached cultures on dishes pretreated with poly-L-ornithine (PLO; Cat# P4957, Sigma) and laminin (Cat# 23017015, Thermo Fisher). The GBM growth medium consisted of Neurobasal medium (Cat# 21103049, Gibco) supplemented with N2 (Cat# 17–502-049, Gibco), B27 (Cat# 12587010, Gibco), nonessential amino acids (Cat# 11140050, Gibco), and GlutaMax (Cat# 35050061, Gibco). Twenty ng/mL recombinant basic Fibroblast Growth Factor (bFGF; Cat# 233-FB-01M, R&D) and 20 ng/mL Epidermal Growth Factor (EGF; Cat# 236-EG- 01M, R&D) were added to the medium every other day. Parental tumors of these patient-derived cultures underwent DNA methylation, mutational and copy number variation profiling (Table S1).[37] All tumors used for PDGCs had a wild-type (WT) IDH genetic background.

Human embryonic stem cell (WA09)-derived NSCs were established and maintained in Dulbecco's modified Eagle Medium: Nutrient Mixture F12 (DMEM F12; Cat#11330057, Thermo Fisher) supplemented with N2, B27, glucose (Cat# A2494001, Thermo Fisher), and bovine insulin (Cat# I0516, Sigma-Aldrich).[16] HEK293T (Cat# 632180, Takara) cells were cultured in Dulbecco's modified Eagle's medium (DMEM; Cat# 11965–118, Gibco) supplemented with 10% fetal bovine serum (FBS; Cat# PS-FB2, Peak Serum) and sodium pyruvate (Cat# 11360070, Gibco). NHAs (Cat# CC-2565, Lonza) were cultured in PLO/laminin-coated tissue culture plates in DMEM media with 10% FBS and N2 supplement. U-87 MG cells (Cat#HTB-14, ATCC) were cultured in Eagle's Minimum Essential Medium (EMEM; Cat# 30–2003, ATCC) supplemented with 10% FBS. All cells were cultured in humidified cell culture incubators at 37°C balanced with 5% $CO_2$ and at 21% $O_2$.

***In vivo* GBM xenografts—**Mice were housed within NYU Langone Medical Center's Animal Facilities. All animal procedures were performed according to an IACUC-approved protocol. Orthotopic intracranial xenografts were performed.[90] Equal numbers of male and female immunodeficient NSG (NOD.Cg-*Prkdc*$^{scid}$ *Il2rg*$^{tm1Wjl}$/SzJ) mice (6–8 weeks of age) were anesthetized with intraperitoneal injection of ketamine/xylazine (10 mg/kg and 100 mg/kg, respectively). A midline skin incision was made and a small hole was drilled through the skull 2 mm off the midline and 2 mm anterior to the coronal suture. Mice were then stereotactically injected with $2.5 \times 10^5$ GBM cells lentivirally infected with a luciferase-containing plasmid. The skin incision was sutured and animals were closely monitored during the recovery period. Mice were weighed every week and sacrificed once they had lost 20% of their maximum body weight or according to ethical guidelines.

## METHOD DETAILS

**Flow cytometry surface staining—**Cells were enzymatically dissociated using Accutase and $5 \times 10^5$ cells were pelleted at 1000 rpm for 5 min. Cells were washed in Dulbecco's phosphate-buffered saline (DPBS; Cat# 14190–144, Gibco) before resuspension in fluorescence-activated cell sorting (FACS) buffer [0.5% BSA (Cat# A3733–100G, Sigma) in DPBS with 2 mM EDTA (Cat#AM9260G, Thermo)] with diluted primary antibody for 30 min at 4°C. Cells were washed in FACS buffer before a final resuspension in FACS buffer and subsequent transfer to a 5 mL round bottom polysterene test tube through a cell strainer (Cat# 352235, Falcon). Samples were run on a BD LSRFortessa (BD Biosciences). Allophycocyanin (APC)- and fluorescein isothiocyanate (FITC)-conjugated primary antibodies were used for staining against CD97, CD55, and THY1/CD90 based on their commercial availability and high detectability.

**Immunofluorescent staining of tissue—**GBM tumors were collected as surgical specimens and normal brain tissue was collected from patients *postmortem*. Tissues were washed for paraffin-embedding and sectioning by the Center for Biospecimen Research & Development (CBRD) core at NYU. Slides were deparaffinized and rehydrated by submersion into xylene (15 min) (Cat# 1330–20-7, Crystalgen), 100% ethanol (3 min) (Cat# UN1170, Fisher bioreagents), 95% ethanol (3 min) (Cat# E7148–500ML, Sigma-Aldrich), and 70% ethanol (5 min) (Cat# 2401, Decon Laboratories). The slides were washed three times in DPBS with 0.1% Tween 20 (PBS-T; Cat# H5151, Promega). Antigen retrieval

was performed by submerging the slides in citrate buffer [2.94 g sodium citrate tribasic dihydrate (Cat# S4641–500G, Sigma-Aldrich), 0.5 mL Tween 20, and 1000 mL dd$H_2O$] and microwaving for 10 min at 800 W followed by 10 min at 200 W. The slides were then allowed to cool slowly at room temperature and were washed three times with PBS-T. Slides were blocked for 30 min using 50 μL normal goat serum (Cat# ab7481, Abcam) in 1 mL DPBS. Slides were then stained with primary antibody solution at 4°C overnight. Slides were then washed three times with PBS-T and stained with secondary antibody for 1 h at room temperature in the dark. Slides were washed, stained with 1:2000 Hoechst 33342 dye (Cat# H3570, Life Technologies) or 100X DAPI (Cat# D8417–1MG, Sigma) in DPBS, covered in ProLong gold antifade reagent (Cat# P36934, Thermo), and mounted with a coverslip (Cat# 10813, Ibidi) for imaging.

**Plasmids and molecular cloning—**All overexpression plasmids were based on the lentiviral vector pCW57-RFP-P2A-MCS (Plasmid #78933, Addgene). ΔPS CD97 was generated using primers against the CD97 isoform 3 expression vector and was assembled using Gibson Assembly. Short hairpin RNAs were cloned cloning into the pRSI9-U6-(sh)-UbiC-TagRFP-2A-Puro (Plasmid #28289, Addgene) shRNA expression vector.[26] Guide RNAs were designed using Benchling, selected based on off-target scores, and cloned into the LentiCRISPRV2-mCherry (Plasmid# 99154, Addgene) backbone. The $MEK^{DD}$ construct was in a pBabe-neomycin (Plasmid #1767, Addgene) expression vector.

**Lentiviral infection and transfection—**Cells were transduced using lentivirus.[91] Lentivirus was produced by co-transfecting HEK293T cells with expression plasmids of interest and packaging plasmids psPax2 and pMD2.G. Lentivirus was collected from the cell culture supernatant 24, 48, and 72 h after transfection and concentrated using the Lenti-X concentrator (Cat# 631231, Contech Takara). For lentiviral transduction, GBM, or NHA medium was supplemented with 4 μg/mL protamine sulfate and cells were treated with viral particles at a multiplicity of infection (MOI) of three. Infected cells were isolated by FACS with the SH800Z sorter (Sony Biotechnology) or by puromycin selection (5 μg/mL). Doxycycline induction was done by adding 1 μg/mL doxycycline to the medium. HEK293T cells were transfected with plasmid DNA using Lipofectamine 2000 (Cat# 11668–019, Invitrogen), following the manufacturer's protocol.

**Immunoblot staining & sample deglycosylation—**Cell medium was aspirated and cells were washed with DPBS (Cat# 14190–250, Gibco). RIPA buffer (Cat# 89901, Thermo) with Protease/Phosphatase inhibitor (Cat# 88669, Fisher) was added directly to cells, which were incubated on ice for 15 min. A cell scraper was used to collect the whole cell lysate, which was transferred to a 1.5 mL tube (Cat# C2170, Thomas Scientific). Samples were sonicated (ON: 15s, OFF: 60s, 8 cycles, High setting, 4°C) using a Bioruptor300 (Diagrenode). Samples were spun at 15000 rcf for 10 min at 4°C and the supernatant was transferred to a fresh tube. If samples were deglycosylated, the Protein Deglycosylation Mix II (Cat# P6044, NEB) was used according to the manufacturer's protocol and samples were incubated at 25°C for 30 min and at 37°C for 16 h. Bovine serum albumin (BSA) protein standards and a detergent compatible (DC) Protein Assay Kit (Cat# 5000112, BioRad) were used to measure protein concentrations of the whole cell lysates according to the

manufacturer's protocol. Up to 40 μg whole cell lysate was mixed in 4X Laemmli Buffer (Cat# 1610747, BioRad) and run in a 12% Mini-PROTEAN TGX Precast Protein Gel (Cat# 4561044, BioRad) for 1 h at 120 V. Protein gels were then transferred to a PVDF membrane (Cat# 1620177, BioRad) for 2 h at 90 V at 4°C. Membranes were blocked [2% BSA in tris-buffered saline with 0.1% Tween 20 (TBS-T)] for 1 h at room temperature. Membranes were stained with primary antibody overnight at 4°C. Membranes were then washed three times in TBS-T for 5 min before incubation with a secondary antibody for 1 h at room temperature in the dark. The membrane was finally washed three times in TBS-T for 5 min and imaged using an iBrightFL1000 (Invitrogen). Bands for non-phosphorylated species were imaged using fluorescent secondary antibodies and by measuring fluorescent signal. Bands for phosphorylated species were imaged using an HRP-conjugated antibody and by measuring chemiluminescent signal using appropriate West Pico PLUS chemiluminescent substrates (Cat# 34577, Thermo) according to the manufacturer's protocol.

**Hoechst staining—**Cells were resuspended (7 days post infection) in DPBS with 1:1000 Hoechst 33342 dye and incubated at 37°C for 30 min. Cells were spun down and resuspended in FACS buffer and transferred to tubes for flow cytometry.

**Annexin-V staining—**One million cells were pelleted (7 days post infection) and washed once in DPBS and then washed once in 1X Binding Buffer (Cat# BMS500BB, eBioscience) in dd$H_2O$. Cells were resuspended in 100 μL 1X Binding Buffer with 5 μL Annexin-V eFluor450 (Cat# 88–8006-74, eBioscience) and were incubated for 15 min in the dark at room temperature. Three hundred μL 1X Binding Buffer was added to the cells and they were spun down and resuspended in 200 μL 1X Binding Buffer with 100X DAPI solution. After a 10-min incubation in the dark at room temperature, cells were resuspended in FACS buffer and transferred to a tube for flow cytometry. Cells that were incubated at 56°C for 20 min were used a positive control for non-viable cells. Cells that were either Annexin-V positive (PE-Cy7) and/or DAPI (Pacific Blue) positive were considered non-viable.

**Transwell migration assay—**PDGCs were dissociated using Accutase and counted (4 days post infection). The cells were resuspended to a concentration of 50,000 cells/100 μL in serum-free Neurobasal media. Meanwhile a 1:30 Matrigel (Cat# 354277, Thermo) to Neurobasal medium solution was made and added to the top well of a transwell permeable support 24-well plate (Cat# 3422, costar) and incubated at room temperature for 2 h. The Matrigel solution was aspirated and the well was washed once with DPBS. One hundred μL of cells were added to the top well. The bottom well was filled with 600 μL of Neurobasal medium with 10% FBS. The plate was incubated at 37°C for 24 h. After 24 h, the media was aspirated and replaced with medium containing 1:1000 Hoechst 33342 dye and was incubated for 10 min at 37°C. The media was then aspirated and replaced with DPBS. Three fluorescent images were taken of the cells on the membrane (total cells). The cells in the upper portion of the well were gently removed using a cotton swab. Three fluorescent images were taken of the remaining cells in the lower portion of the well (migrated cells). The fluorescent intensity was measured and the fraction of migrated cells to total cells was calculated.

**Tumorsphere formation assay—**Cells were enzymatically dissociated using Accutase and counted using Countess II (Invitrogen). Cells were spun down at 1000 rpm for 5 min and brought to a concentration of 100–500 cells/50 μL. One row (12 wells) of a 96-well plate (Cat# 7200656, Fisher) were filled with 50 μL of the cell suspension. Cells were fed every two days with EGF and bFGF supplements and were given 14 days to form tumorspheres. Ninety-six-well plates were then scanned using an Evos Cell Imaging System (Evos) and tumorspheres were counted using ImageJ software.

**Extreme limiting dilution assays (ELDA)—**Short hairpin RNA transduced PDGCs were dissociated using Accutase and counted. Cells were plated in 24 wells of a 96-well plate at four separate concentrations: 1000 cells/well, 300 cells/well, 30 cell/well, and 3 cells/well. Cells were then fed every two days and given 14 days to grow. The number of completely empty wells were recorded. Clonogenic frequencies were calculated using ELDA software (https://bioinf.wehi.edu.au/software/elda/). For plotting, the $\log_{10}$ of each frequency was taken.

**Cell competition assay—**GBM cells were lentivirally infected with a LentiCRISPRv2 gRNA:Cas9:mCherry construct with an MOI of 3. Cells were then enzymatically dissociated using Accutase into single cells and counted. We mixed 100,000 infected, mCherry+ cells with 100,000 uninfectedcells. Flow cytometry [BD LSRFortessa (BD Biosciences)] was used to measure the initial proportion of mCherry+ cells. Every four days, tumorspheres were enzymatically dissociated, the proportion of mCherry+ cells was measured via flow cytometry, and 100,000 cells were replated. This was done until day 20.

**Luciferase assay—**PDGCs lentivirally infected with a dox-inducible CD97-overexpression or empty vector were transfected with luciferase signaling-reporter plasmids: cAMP response element–Luciferase (Cat# E8471, Promega), SRE-Luciferase (Cat# E1340, Promega), SRF-RE-Luciferase (Cat# E1350, Promega), and NFAT-RE-Luciferase (Cat# E8481, Promega). Twenty-four hours after transfection, cells were reseeded in black 96-well plates at a density of 75,000 cells per well with medium containing doxycycline (or dox-free medium). Forty-eight hours after transfection, cells were lysed and luciferase activity was detected using the Bright-Glo Luciferase assay system (Cat# E2650, CisBio) and a BioTek Synergy H1 microplate reader according to the manufacturer's protocol.

**IVIS imaging of *in vivo* GBM xenografts—***In vivo* GBM xenografts were monitored using an IVIS Lumina XR (PerkinElmer).[92] First, mice were weighed and injected intraperitoneally with 10 μL/g body weight Luciferin substrate solution [D-Luciferin Potassium Salt (LUCK-300, Gold Biotechnology) diluted in DPBS to a final concentration of 20 mg/mL]. Mice were anesthetized using isoflurane and inserted into the IVIS imaging system. Thirteen minutes after Luciferin injection, mice were imaged at a 150 s exposure time. Living Image software (PerkinElmer) was used to quantify the "Radiance (Photons)" within the selected ROI.

**Bulk RNA-sequencing—**Three replicates of a PDGC (knockdown, scrambled, overexpression, and empty vector) and one replicate each of three PDGCs (knockdown and scrambled) were plated adherently in a 6-well plate. Two replicates of NSCs were

also plated adherently on a 6-well plate. RNA was extracted using a RNeasy Mini Kit (Cat# 74104, Qiagen) according to the manufacturer's protocol. Samples were submitted to the NYU Langone Genome Technology Core (GTC) for sequencing on an Illumina NovaSeq 6000 flow cell. FastQ files were aligned to the reference genome (hg19) using the splice aware aligner STAR (v2.5.0c), and the read counts were generated. DESeq2 was used for normalization, differential gene expression analysis, and to generate volcano plots. Log-processed reads per kilobase per million mapped reads (RPKM) values were used to generate a heatmap of aGPCR expression in GBM cells using Seq-N-Slide (rna-star-groups-dge) software. Peaks were visualized at the *CD97* locus (chr19:14488844–14534630; hg19 reference genome) using the WashU Epigenome Browser (http://epigenomegateway.wustl.edu/browser/) and Integrative Genomics Viewer (IGV).

**Single-cell 10X multiome (ATAC + RNA) sequencing—**Fresh IDH-mutant astrocytoma and IDH-wildtype GBM surgical specimens were immediately flash frozen in liquid nitrogen. Tissue was homogenized using a pestle (Cat#12–141-367; Thermo). The sample was then processed according to the "10X Genomics Nuclei Isolation from Complex Tissues for Single Cell Multiome ATAC + GEX Sequencing Demonstrated Protocol CG000375 Rev B" protocol and nuclei were processed for sequencing on an Illumina NovaSeq 6000 flow cell. Data were processed, normalized, integrated for the two specimens, and clustered using Seurat and Signac packages based on RNA and ATAC peak data in R. Only cells with 500–5000 features and with a percentage of mitochondrial genes less than 15% were included in the analysis. Clusters were identified based on the expression of relevant markers (neuronal, oligodendrocytic, astrocytic, and immune) and based on upregulated enriched pathways determined by GO. Oligodendrocytic and neuroglial clusters were compiled together as "Normal brain cells". Immune populations from the two datasets were clustered together as "Immune cells". IDH-mutant astrocytoma and IDH-wildtype GBM clusters were identified by their high astrocytic expression profile along with high expression of other oncogenic markers (*EGFR*, *TIMP3*, *SOX2*, *TUBA1A*, *MYC*, *HIF1A*, *FN1*, *HK2*, *TMOD1*, and *IGFBP5*). ATAC-seq data was visualized at the *CD97* locus (chr19:14380000–14420000; hg38 reference genome) for the clusters using the Signac package in R.

**Pathway enrichment analysis & correlation matrix analysis—**Differentially expressed downregulated genes were plugged into GO PANTHER software (http://pantherdb.org/). The top 10 depleted pathways upon CD97 knockdown were plotted based on $\log_{10}$(fold enrichment) values. GSEA software (https://www.gsea-msigdb.org/gsea/index.jsp) was used to generate GSEA plots from gene count data. DGCA in R was used to generate a correlation matrix based on RNA-seq data after CD97 knockdown or overexpression in PDGC replicates. Genes designated as glycolytic stem from GO:0061621 along with select glucose transporters. Genes designated as TCA-cycle/OXPHOS include those from GO:0006099 and all cytochrome oxidase subunits. Positive integers designate positive correlation in gene expression patterns, while negative integers designate negative correlation in gene expression patterns.

## Steady-state metabolomics & glucose tracing

**Steady-state metabolomics:** Three replicates of two PDGCs (knockdown and scrambled) were plated non-adherently on 6-well plates. After two days, all cells were collected into a 1.5 mL tube and spun at 3000 rcf for 1 min at 4°C. The supernatant was aspirated and cells were washed in 1 mL of DPBS and immediately pelleted again. Cell pellets were flash-frozen and submitted to the Metabolomics Laboratory for hybrid metabolomics analysis using liquid chromatography/mass spectrometry (LC-MS/MS). A more detailed description of the methods performed for metabolite extraction, LC-MS/MS hybrid metabolomics, and relative metabolite quantification is provided in Supplementary Methods. One replicate was excluded for technical reasons.

**Glucose tracing:** Three replicates of a PDGC were plated on 6-well plates (knockdown and scrambled). Cells were given fresh Neurobasal-A medium, no D-glucose, no sodium pyruvate (Cat# A2477501, Thermo) with 25 mM [U-$^{13}C_6$]-glucose (Cat# 389374–10.00G, Sigma). Triplicates were collected and spun at 3000 rcf for 1 min at 4 °C at three separate timepoints (5, 30, & 120 min). Cell pellets were washed with 1 mL DPBS and flash-frozen. Tubes were submitted to the Metabolomics Laboratory for hybrid metabolomics analysis using LC-MS/MS.

**Extraction of metabolites:** Prior to extraction, samples were moved from −80°C storage to wet ice and thawed. Extraction buffer, consisting of 80% methanol (Cat# 615130025, Thermo Fisher) and 500 nM metabolomics amino acid mix standard (Cat# MSK-A2–1.2, Cambridge Isotope Laboratories), was prepared and placed on dry ice. Samples were extracted by mixing 50 μL of sample with 950 μL of extraction buffer in 2.0 mL screw cap vials containing ~100 μL of disruption beads (Cat# 9835, Research Products International). Each sample was homogenized for 10 cycles on a BeadBlaster homogenizer (Benchmark Scientific). Cycling consisted of a 30 s homogenization time at 6 m/s followed by a 30 s pause. Samples were subsequently spun at 21,000 rcf for 3 min at 4°C. A set volume of each (450 μL) was transferred to a 1.5 mL tube and dried down by SpeedVac (Thermo Fisher). Samples were reconstituted in 50 μL of Optima LC/MS grade water (Cat# W6500, Fisher Scientific). Samples were sonicated for 2 min, then spun at 21,000 rcf for 3 min at 4°C. Twenty μL were transferred to LC vials containing glass inserts for analysis. The remaining sample was placed in −80°C for long term storage.

**LC-MS/MS with the hybrid metabolomics method:** Samples were subjected to an LC-MS analysis to detect and quantify known peaks. A metabolite extraction was carried out on each sample.[93] The LC column was a Millipore ZIC-pHILIC (2.1 × 150 mm, 5 μm) coupled to a Dionex Ultimate 3000 system and the column oven temperature was set to 25°C for the gradient elution. A flow rate of 100 μL/min was used with the following buffers; A) 10 mM ammonium carbonate in water, pH 9.0, and B) neat acetonitrile. The gradient profile was as follows; 80–20% B (0–30 min), 20–80% B (30–31 min), 80–80% B (31–42 min). Injection volume was set to 2 μL for all analyses (42 min total run time per injection). MS analyses were carried out by coupling the LC system to a Thermo Q Exactive HF mass spectrometer operating in heated electrospray ionization mode (HESI). Method duration was 30 min with a polarity switching data-dependent Top 5 method for both positive and negative modes.

Spray voltage for both positive and negative modes was 3.5 kV and capillary temperature was set to 320°C with a sheath gas rate of 35, aux gas of 10, and max spray current of 100 μA. The full MS scan for both polarities utilized 120,000 resolution with an AGC target of 3e6 and a maximum IT of 100 ms, and the scan range was from 67 to 1000 m/z. Tandem MS spectra for both positive and negative mode used a resolution of 15,000 AGC target of 1e5, maximum IT of 50 ms, isolation window of 0.4 m/z, isolation offset of 0.1 m/z, fixed first mass of 50 m/z, and 3-way multiplexed normalized collision energies (nCE) of 10, 35, 80. The minimum AGC target was 1e4 with an intensity threshold of 2e5. All data were acquired in profile mode.

**Relative quantification of metabolites:** The resulting ThermoTM RAW files were converted to mzXML format using ReAdW.exe version 4.3.1 to enable peak detection and quantification. The centroided data were searched using an in-house python script Mighty_skeleton version 0.0.2 and peak heights were extracted from the mzXML files based on a previously established library of metabolite retention times and accurate masses adapted from the Whitehead Institute,[94] and verified with authentic standards and/or high-resolution MS/MS spectral manually curated against the NIST14 MS/MS[95] and METLIN (2017)[96] tandem mass spectral libraries. Metabolite peaks were extracted based on the theoretical m/z of the expected ion type e.g., [M + H]+, with a ±5 part-per-million (ppm) tolerance, and a ±7.5 s peak apex retention time tolerance within an initial retention time search window of ±0.5 min across the study samples. The resulting data matrix of metabolite intensities for all samples and blank controls was processed with an in-house statistical pipeline Metabolyze version 1.0 and final peak detection was calculated based on a signal to noise ratio (S/N) of 3X compared to blank controls, with a floor of 10,000 (arbitrary units). For samples where the peak intensity was lower than the blank threshold, metabolites were annotated as not detected, and the threshold value was imputed for any statistical comparisons to enable an estimate of the fold change as applicable. The resulting blank corrected data matrix was then used for all group-wise comparisons, and t-tests were performed with the Python SciPy (1.1.0)[97] library to test for differences and generate statistics for downstream analyses. Any metabolite with p value <0.05 was considered significantly regulated (up or down).

**Lactate assay—**Lentivirally infected GBM cells were plated on PLO/laminin treated 6-well plates in 1 mL of GBM medium and given 24 h to grow. A lactate assay cocktail was made [50% Glycine/Hydrazine 0.6M solution (Cat# G5418, Sigma), 1% 240 mM NAD+ (Cat# N0632, Sigma), 2 μL/mL Lactate Dehydrogenase (5U/uL) (Cat# 10127230001, Roche), 49% sterile dd$H_20$]. A series of lactate standards ranging from 10 mM to 0 mM were made (Cat# AC18987–0050, Fisher). Two hundred μL of the lactate cocktail was added to the wells of a 96-well plate. Five μL of each standard or sample was added in triplicates to the wells containing the lactate cocktail. The solution was mixed and incubated for 1 h at 37°C. The solution was mixed again and the absorbance at 340 nm was read using a Synergy H1 Plate Reader (BioTek).

**Seahorse Cell Energy Phenotype assay—**Seahorse XFe24 Analyzer (Agilent) and the Seahorse XF Cell Energy Phenotype Test Kit (Cat# 103325–100, Agilent) were used to

perform assays according to the manufacturer's protocol. In brief, a Seahorse cell culture plate was treated with PLO/laminin and 10,000 dissociated GBM cells were plated per well, with five technical replicates per condition accompanied with a blank control well. Cells were incubated overnight at 37°C in a $CO_2$ incubator to allow for attachment. Meanwhile, a Seahorse Utility plate/sensor cartridge was hydrated and calibrated using Calibration buffer (Cat# 100840–000, Agilent) in a non-$CO_2$ incubator at 37°C overnight. Cell medium was aspirated and replaced with 500 μL Assay medium [Agilent Base Medium (Cat# 102353–100, Agilent), 1 mM pyruvate (Cat# 103578–100, Agilent), 2 mM glutamine (Cat# 103579–100, Agilent), 10 mM glucose (Cat# 103577–100, Agilent)] and was incubated for 1 h in a non-$CO_2$ incubator at 37°C. The mitochondrial stressors carbonyl cyanide p-(tri-fluoromethoxy)phenyl-hydrazone (FCCP) and oligomycin were prepared to a final molar concentration of 1.25 μM and 10 μM, respectively, and were added to Port A of the sensor cartridge. The Seahorse cell plate and sensor cartridge were run on a Seahorse XF Cell Energy Phenotype Assay program using Agilent Wave software. Both OCR and ECAR were measured at three baseline timepoints and six timepoints after the addition of the mitochondrial stressors.

**MEK mutant transfection & selection—**GBM cells were transfected with the neomycin-resistant $MEK^{DD}$ construct or a neomycin-resistant empty vector control using Lipofectamine Stem Transfection Reagent(Cat# STEM00008, Thermo) overnight. Cells were treatedfor three days withmedia containing 1 mg/mL G418 sulfate (Cat# 61–234-RG, Corning) dissolved in DPBS. Cells were given 7–14 days to expand in low dose (100 μg/mL) G418 medium before they were used for specified experiments.

**RHOA-pulldown assay—**The RhoA Pull-down Activation Assay Biochem Kit (Cat# BK036, Cytoskeleton) was ordered and the manufacturer's protocol was followed. Five hundred μg of cell lysate was used and 15 μL beads.

**HTRF-based β-arrestin recruitment assay—**GBM cells overexpressing wildtype CD97, the ΔPS mutant, or an empty vector control were plated (50,000 cells/well) on a PLO/laminin coated white 96-well plate. A homogeneous time-resolved fluorescence (HTRF)-based β-arrestin2 recruitment kit was used and followed according to the manufacturer's protocol (Cat# 62BDBAR2PEB, cisbio). HTRF values were measured using a FlexStation 3 Multi-Mode Microplate Reader (Molecular Devices).

**Ligand-based immunoblots—**Six-well plates were coated with PLO/laminin. Wells were then additionally coated with recombinant human CD55 (Cat# 2009-CD-050, R&D) or recombinant human THY1/CD90 (Cat# 16897-HCCH, Sino Biological) at a concentration of 24 μg/mL overnight. GBM cells overexpressing CD97 or an empty vector control were seeded (~$1 \times 10^6$ cells/well) on the plate. Whole cell lysates were collected for immunoblotting 24 h after seeding.

**Generation of antibody-drug conjugate (ADC) against CD97—**The gene encoding the ectodomain of CD97 isoform 1 was synthesized (Integrated DNA Technologies) and cloned into the mammalian expression vector pBCAG.[98,99] The expi293F cells (Thermo Fisher) were transfected with the vector using the ExpiFectamine 293 Transfection Kit

(Thermo Fisher) according to the manufacturer's protocol. The CD97 protein was purified from the cell culture supernatant by immobilized metal affinity chromatography (IMAC) followed by size exclusion chromatography. The sorting of a synthetic human antibody (sAb) library and identification of anti-CD97 sAb by phage ELISA were performed essentially as described previously.[100,101] The gene encoding the VH domain of the antibody was cloned into a modified version of pFUSEss-CHIg-hG1 (InvivoGen) harboring the LALA-PG (L234A, L235A, P329G) mutations that abrogate Fc receptor binding,[102] and the gene encoding the VL domain into pFUSEss-CLIg-hk (InvivoGen). The antibody in this IgG1-LALA-PG format was produced using the expiCHO expression system according to the manufacturer's protocol (Thermo Fisher), and purified with Protein A affinity chromatography. The drug conjugation reaction was performed as described previously.[103] Briefly, the interchain disulfide bonds of the antibody were cleaved with DTT. A 9.5-fold molar excess of MC-Val-Cit-PAB-MMAF (BOC Science) was added to the reduced antibody, and after 1 h of incubation, the reaction was quenched by adding excess cysteine. The excess drug and cysteine were removed with the Zeba spin desalting column (Thermo Fisher). Approximately 6–7 drug molecules were conjugated per antibody.

**Antibody internalization assay—**Two PDGCs were seeded in 96-well plates in triplicates. Antibodies were conjugated with the pHAb amine reactive dye (Cat# G9841, Promega) according to the manufacturer's protocol. Dye-conjugated antibodies were purified using the Capturem Protein G miniprep columns (Cat# 635725, Takara). Purified antibodies were dialyzed into DPBS overnight. The concentration of both the anti-CD97 antibody and the isotype control used for the assay was 30 μg/mL and the cells were incubated for 20 h. The cells were then harvested and analyzed by flow cytometry to determine internalization. The pH sensitive pHAb dye that is conjugated to each antibody has low or no fluorescence (PE channel) at pH > 7. Upon internalization, the dye becomes fluorescent at an acidic pH present in early endosomes and lysosomes. The increase in mean fluorescence intensity was measured via the PE channel.

**Antibody-drug conjugate dose-response curves—**Ninety-six-well plates were coated with PLO/laminin. We then plated $10^4$ cells per well (100 μL per well; each condition in triplicates) and allowed them to adhere overnight. Serial dilutions of ADC, MMAF, and MMAE were prepared in appropriate cell medium to give the following final concentrations: 150 nM, 30 nM, 6 nM, 1.2 nM, 240 p.m., 50 p.m., 10 p.m., 3 p.m., 1.4 p.m., and 0. Ten μL from dilutions were added to wells. On the seventh day, cells were stained using 1:2000 Hoechst 33342 dye (Cat# H3570, Life technologies) and representative images were taken. Ten μL of WST8 (Cat# ab228554, Abcam) was added to each well and the absorbance at 460 nm was measured using a Synergy H1 Plate Reader (BioTek) after a 3-h incubation at 37°C. Dose-response curves and respective $LD_{50}$ curves were generated using GraphPad Prism software (version 8.4.3). Curves were based on a nonlinear regression fit.

**Databases used and data availability—**The Allen Brain Map Human M1 10X Transcriptomics Explorer database was used to visualize expression levels in normal human brain cells. Proteomic data for normal brain was collected and annotated as in Perna et al.[34] "Not detected" indicates expression below the level of mass

spectrometry sensitivity. Expression values within one standard deviation were considered to be of “Medium” abundance, Expression values above this threshold were considered to be of “High” abundance. Expression values below one standard deviation were considered to be of “Low” abundance. Publicly available H3K27ac ChIP-seq from the Gene Expression Omnibus (GEO) was displayed via the Integrative Genomics Viewer (IGV) (https://software.broadinstitute.org/software/igv/). Peaks associated around the *CD97* locus (chr19:14488844–14534630; hg19 reference genome) are shown for all specimens [IDH-WT GBM: GSM1824800, GSM1824811; IDH-mutant anaplastic astrocytoma: GSM1824813, GSM1824808 (anaplastic astrocytoma)]. GBM phosphoproteomic and proteomic data were from the GBM datasets of the Clinical Proteomic Tumor Analysis Consortium (CPTAC) included in Wang et al. analyzing multi-omic profiles from 99 treatment-naïve GBM specimens.[35] Publicly available single-cell RNA-seq data of adult and pediatric glioblastoma from the Broad Institute Single Cell Portal (GSE131928) were used to look at expression of *CD97* and its putative ligands *THY1/CD90* and *CD55*. Bulk RNA-sequencing and single cell RNA/ATAC-sequencing data have been deposited at GEO under GSE230393 and GSE230389 accession numbers, respectively.

### QUANTIFICATION AND STATISTICAL ANALYSIS

All experiments were performed in biological replicates of at least three repeats unless otherwise specified. Statistical analysis was performed using GraphPad Prism (version 8.4.3). Summary statistics are represented as mean ± standard error of the mean (SEM) unless otherwise indicated. Statistical significance was calculated using either Students t-test, log -rank test (for Kaplan-Meier survival curves), 1-way analysis of variance (ANOVA), or two-way ANOVA, with Tukey’s or Sidak’s *post hoc* test for multiple comparisons. p values $< 0.05$ were considered statistically significant (*, $p < 0.05$; **, $p < 0.01$; ***, $p < 0.001$; ****, $p < 0.0001$).

## Supplementary Material

Refer to Web version on PubMed Central for supplementary material.

## ACKNOWLEDGMENTS

We thank the Genome Technology Center, the Microscopy Core, the Flow Cytometry Core, the Research Support Service, the Applied Bioinformatics Laboratory, the Center for Biospecimen Research and Development (CBRD) Core, the Vilcek Institute, the Skirball Mouse Facility, and the Metabolomic Laboratory at the NYU Grossman School of Medicine. We also thank Drs. Kiyomi Araki and Ben Néel for sharing $MEK^{DD}$ constructs; Dr. Iannis Aifantis and his lab members for use of lab equipment; and Dr. Daniel Orringer for providing one of the surgical specimens. We also thank the Allen Brain Atlas, the Broad Institute, and the GEO for their commitment to providing publicly accessible data. This study was supported by NIH/NINDS R01 NS102665, R01 NS124920, and R21 NS126806 and NYSTEM (NY State Stem Cell Science) IIRP C32595GG to D.G.P.; by R21 CA246457 to T.H.; and by R01 CA251669 to S.K. and C.Y.P. D.G.P. was also supported by NIH/NIBIB R01 EB028774, NIH/NCI R21CA263402, NIH/NCATS 2UL1TR001445, the NYU Grossman School of Medicine, and DFG (German Research Foundation) FOR2149. N.R.-B. was supported by an NYSTEM Institutional training grant (#C322560GG) and an NIH Cell Biology Graduate Student Training Grant (T32GM136542). Core facilities were supported in part by Cancer Center Support Grant P30CA016087 to the Perlmutter Cancer Center of the NYU Grossman School of Medicine.

## INCLUSION AND DIVERSITY

One or more of the authors of this paper self-identifies as a member of the LGBTQIA+ community. We support inclusive, diverse, and equitable conduct of research.

## REFERENCES


1. Ceccarelli M, Barthel FP, Malta TM, Sabedot TS, Salama SR, Murray BA, Morozova O, Newton Y, Radenbaugh A, Pagnotta SM, et al. (2016). Molecular Profiling Reveals Biologically Discrete Subsets and Pathways of Progression in Diffuse Glioma. Cell 164, 550–563. 10.1016/j.cell.2015.12.028. [PubMed: 26824661]
2. Verhaak RGW, Hoadley KA, Purdom E, Wang V, Qi Y, Wilkerson MD, Miller CR, Ding L, Golub T, Mesirov JP, et al. (2010). Integrated genomic analysis identifies clinically relevant subtypes of glioblastoma characterized by abnormalities in PDGFRA, IDH1, EGFR, and NF1. Cancer Cell 17, 98–110. 10.1016/j.ccr.2009.12.020. [PubMed: 20129251]
3. Ostrom QT, Gittleman H, Farah P, Ondracek A, Chen Y, Wolinsky Y, Stroup NE, Kruchko C, and Barnholtz-Sloan JS (2013). CBTRUS statistical report: Primary brain and central nervous system tumors diagnosed in the United States in 2006–2010. Neuro Oncol. 15, ii1–ii56. 10.1093/neuonc/not151. [PubMed: 24137015]
4. Stupp R, Mason WP, van den Bent MJ, Weller M, Fisher B, Taphoorn MJB, Belanger K, Brandes AA, Marosi C, Bogdahn U, et al. (2005). Radiotherapy plus concomitant and adjuvant temozolomide for glioblastoma. N. Engl. J. Med. 352, 987–996. 10.1056/NEJMoa043330. [PubMed: 15758009]
5. Louis DN, Perry A, Wesseling P, Brat DJ, Cree IA, Figarella-Branger D, Hawkins C, Ng HK, Pfister SM, Reifenberger G, et al. (2021). The 2021 WHO Classification of Tumors of the Central Nervous System: a summary. Neuro Oncol. 23, 1231–1251. 10.1093/neuonc/noab106. [PubMed: 34185076]
6. Stephan G, Ravn-Boess N, and Placantonakis DG (2021). Adhesion G protein-coupled receptors in glioblastoma. Neurooncol. Adv. 3, vdab046. 10.1093/noajnl/vdab046. [PubMed: 33959717]
7. Krishnan A, Nijmeijer S, de Graaf C, and Schiöth HB (2016). Classification, Nomenclature, and Structural Aspects of Adhesion GPCRs. Handb. Exp. Pharmacol. 234, 15–41. 10.1007/978-3-319-41523-9_2. [PubMed: 27832482]
8. Hamann J, Aust G, Araç D, Engel FB, Formstone C, Fredriksson R, Hall RA, Harty BL, Kirchhoff C, Knapp B, et al. (2015). International Union of Basic and Clinical Pharmacology. XCIV. Adhesion G protein-coupled receptors. Pharmacol. Rev. 67, 338–367. 10.1124/pr.114.009647. [PubMed: 25713288]
9. Liebscher I, Schön J, Petersen SC, Fischer L, Auerbach N, Demberg LM, Mogha A, Cöster M, Simon KU, Rothemund S, et al. (2014). A tethered agonist within the ectodomain activates the adhesion G protein-coupled receptors GPR126 and GPR133. Cell Rep. 9, 2018–2026. 10.1016/j.celrep.2014.11.036. [PubMed: 25533341]
10. Zhang S, Chatterjee T, Godoy C, Wu L, Liu QJ, and Carmon KS (2019). GPR56 Drives Colorectal Tumor Growth and Promotes Drug Resistance through Upregulation of MDR1 Expression via a RhoA-Mediated Mechanism. Mol. Cancer Res. 17, 2196–2207. 10.1158/1541-7786.Mcr-19-0436. [PubMed: 31444231]
11. Bayin NS, Frenster JD, Kane JR, Rubenstein J, Modrek AS, Baitalmal R, Dolgalev I, Rudzenski K, Scarabottolo L, Crespi D, et al. (2016). GPR133 (ADGRD1), an adhesion G-protein-coupled receptor, is necessary for glioblastoma growth. Oncogenesis 5, e263. 10.1038/oncsis.2016.63. [PubMed: 27775701]
12. Cui H, Yu W, Yu M, Luo Y, Yang M, Cong R, Chu X, Gao G, and Zhong M (2021). GPR126 regulates colorectal cancer cell proliferation by mediating HDAC2 and GLI2 expression. Cancer Sci. 112, 1798–1810. 10.1111/cas.14868. [PubMed: 33629464]
13. Aust G, Eichler W, Laue S, Lehmann I, Heldin NE, Lotz O, Scherbaum WA, Dralle H, and Hoang-Vu C (1997). CD97: a dedifferentiation marker in human thyroid carcinomas. Cancer Res. 57, 1798–1806. [PubMed: 9135025]

14. Ackerman SD, Garcia C, Piao X, Gutmann DH, and Monk KR (2015). The adhesion GPCR Gpr56 regulates oligodendrocyte development via interactions with Gα12/13 and RhoA. Nat. Commun. 6, 6122. 10.1038/ncomms7122. [PubMed: 25607772]

15. Bianchi E, Sun Y, Almansa-Ordonez A, Woods M, Goulding D, Martinez-Martin N, and Wright GJ (2021). Control of oviductal fluid flow by the G-protein coupled receptor Adgrd1 is essential for murine embryo transit. Nat. Commun. 12, 1251. 10.1038/s41467-021-21512-w. [PubMed: 33623007]

16. Modrek AS, Golub D, Khan T, Bready D, Prado J, Bowman C, Deng J, Zhang G, Rocha PP, Raviram R, et al. (2017). Low-Grade Astrocytoma Mutations in IDH1, P53, and ATRX Cooperate to Block Differentiation of Human Neural Stem Cells via Repression of SOX2. Cell Rep. 21, 1267–1280. 10.1016/j.celrep.2017.10.009. [PubMed: 29091765]

17. Modrek AS, Bayin NS, and Placantonakis DG (2014). Brain stem cells as the cell of origin in glioma. World J. Stem Cells 6, 43–52. 10.4252/wjsc.v6.i1.43. [PubMed: 24567787]

18. Lee JH, Lee JE, Kahng JY, Kim SH, Park JS, Yoon SJ, Um JY, Kim WK, Lee JK, Park J, et al. (2018). Human glioblastoma arises from subventricular zone cells with low-level driver mutations. Nature 560, 243–247. 10.1038/s41586-018-0389-3. [PubMed: 30069053]

19. Brennan CW, Verhaak RGW, McKenna A, Campos B, Noushmehr H, Salama SR, Zheng S, Chakravarty D, Sanborn JZ, Berman SH, et al. (2013). The somatic genomic landscape of glioblastoma. Cell 155, 462–477. 10.1016/j.cell.2013.09.034. [PubMed: 24120142]

20. Jaspars LH, Vos W, Aust G, Van Lier RA, and Hamann J (2001). Tissue distribution of the human CD97 EGF-TM7 receptor. Tissue Antigens 57, 325–331. 10.1034/j.1399-0039.2001.057004325.x. [PubMed: 11380941]

21. Hamann J, Veninga H, de Groot DM, Visser L, Hofstra CL, Tak PP, Laman JD, Boots AM, and van Eenennaam H (2010). CD97 in leukocyte trafficking. Adv. Exp. Med. Biol. 706, 128–137. 10.1007/978-1-4419-7913-1_11. [PubMed: 21618832]

22. Spendlove I., and Sutavani R. (2010). The role of CD97 in regulating adaptive T-cell responses. Adv. Exp. Med. Biol. 706, 138–148. 10.1007/978-1-4419-7913-1_12. [PubMed: 21618833]

23. Leemans JC, te Velde AA, Florquin S, Bennink RJ, de Bruin K, van Lier RAW, van der Poll T, and Hamann J (2004). The epidermal growth factor-seven transmembrane (EGF-TM7) receptor CD97 is required for neutrophil migration and host defense. J. Immunol. 172, 1125–1131. 10.4049/jimmunol.172.2.1125. [PubMed: 14707087]

24. Kop EN, Adriaansen J, Smeets TJM, Vervoordeldonk MJ, van Lier RAW, Hamann J, and Tak PP (2006). CD97 neutralisation increases resistance to collagen-induced arthritis in mice. Arthritis Res. Ther. 8, R155. 10.1186/ar2049. [PubMed: 17007638]

25. Aust G, Zheng L, and Quaas M (2022). To Detach, Migrate, Adhere, and Metastasize: CD97/ADGRE5 in Cancer. Cells 11, 1538. 10.3390/cells11091538. [PubMed: 35563846]

26. Martin GH, Roy N, Chakraborty S, Desrichard A, Chung SS, Woolthuis CM, Hu W, Berezniuk I, Garrett-Bakelman FE, Hamann J, et al. (2019). CD97 is a critical regulator of acute myeloid leukemia stem cell function. J. Exp. Med. 216, 2362–2377. 10.1084/jem.20190598. [PubMed: 31371381]

27. Ward Y, Lake R, Yin JJ, Heger CD, Raffeld M, Goldsmith PK, Merino M, and Kelly K (2011). LPA receptor heterodimerizes with CD97 to amplify LPA-initiated RHO-dependent signaling and invasion in prostate cancer cells. Cancer Res. 71, 7301–7311. 10.1158/0008-5472.Can-11-2381. [PubMed: 21978933]

28. Aust G, Steinert M, Schütz A, Boltze C, Wahlbuhl M, Hamann J, and Wobus M (2002). CD97, but not its closely related EGF-TM7 family member EMR2, is expressed on gastric, pancreatic, and esophageal carcinomas. Am. J. Clin. Pathol. 118, 699–707. 10.1309/a6ab-vf3f-7m88-c0ej. [PubMed: 12428789]

29. Safaee M, Clark AJ, Oh MC, Ivan ME, Bloch O, Kaur G, Sun MZ, Kim JM, Oh T, Berger MS, and Parsa AT (2013). Overexpression of CD97 confers an invasive phenotype in glioblastoma cells and is associated with decreased survival of glioblastoma patients. PLoS One 8, e62765. 10.1371/journal.pone.0062765. [PubMed: 23658650]

30. Safaee M, Fakurnejad S, Bloch O, Clark AJ, Ivan ME, Sun MZ, Oh T, Phillips JJ, and Parsa AT (2015). Proportional upregulation of CD97 isoforms in glioblastoma and glioblastoma-derived

brain tumor initiating cells. PLoS One 10, e0111532. 10.1371/journal.pone.0111532. [PubMed: 25714433]

31. Safaee MM, Wang EJ, Jain S, Chen JS, Gill S, Zheng AC, Garcia JH, Beniwal AS, Tran Y, Nguyen AT, et al. (2022). CD97 is associated with mitogenic pathway activation, metabolic reprogramming, and immune microenvironment changes in glioblastoma. Sci. Rep. 12, 1464. 10.1038/s41598-022-05259-y. [PubMed: 35087132]
32. Eichberg DG, Slepak TI, Pascoini AL, Komotar RJ, and Ivan ME (2021). Genetic manipulation of adhesion GPCR CD97/ADGRE5 modulates invasion in patient-derived glioma stem cells. J. Neuro Oncol. 153, 383–391. 10.1007/s11060-021-03778-8.
33. Chidambaram A, Fillmore HL, Van Meter TE, Dumur CI, and Broaddus WC (2012). Novel report of expression and function of CD97 in malignant gliomas: correlation with Wilms tumor 1 expression and glioma cell invasiveness. J. Neurosurg. 116, 843–853. 10.3171/2011.11.Jns111455. [PubMed: 22313360]
34. Perna F, Berman SH, Soni RK, Mansilla-Soto J, Eyquem J, Hamieh M, Hendrickson RC, Brennan CW, and Sadelain M (2017). Integrating Proteomics and Transcriptomics for Systematic Combinatorial Chimeric Antigen Receptor Therapy of AML. Cancer Cell 32, 506–519.e5. 10.1016/j.ccell.2017.09.004. [PubMed: 29017060]
35. Wang LB, Karpova A, Gritsenko MA, Kyle JE, Cao S, Li Y, Rykunov D, Colaprico A, Rothstein JH, Hong R, et al. (2021). Proteogenomic and metabolomic characterization of human glioblastoma. Cancer Cell 39, 509–528.e20. 10.1016/j.ccell.2021.01.006. [PubMed: 33577785]
36. Flavahan WA, Drier Y, Liau BB, Gillespie SM, Venteicher AS, Stemmer-Rachamimov AO, Suva ML., and Bernstein BE. (2016). Insulator dysfunction and oncogene activation in IDH mutant gliomas. Nature 529, 110–114. 10.1038/nature16490. [PubMed: 26700815]
37. Frenster JD, Stephan G, Ravn-Boess N, Bready D, Wilcox J, Kieslich B, Wilde C, Sträter N, Wiggin GR, Liebscher I, et al. (2021). Functional impact of intramolecular cleavage and dissociation of adhesion G protein-coupled receptor GPR133 (ADGRD1) on canonical signaling. J. Biol. Chem. 296, 100798. 10.1016/j.jbc.2021.100798. [PubMed: 34022221]
38. Hsiao CC, Cheng KF, Chen HY, Chou YH, Stacey M, Chang GW, and Lin HH (2009). Site-specific N-glycosylation regulates the GPS auto-proteolysis of CD97. FEBS Lett. 583, 3285–3290. 10.1016/j.febslet.2009.09.001. [PubMed: 19737555]
39. Kathagen-Buhmann A, Schulte A, Weller J, Holz M, Herold-Mende C, Glass R, and Lamszus K (2016). Glycolysis and the pentose phosphate pathway are differentially associated with the dichotomous regulation of glioblastoma cell migration versus proliferation. Neuro Oncol. 18, 1219–1229. 10.1093/neuonc/now024. [PubMed: 26917237]
40. Stanke KM, Wilson C, and Kidambi S (2021). High Expression of Glycolytic Genes in Clinical Glioblastoma Patients Correlates With Lower Survival. Front. Mol. Biosci. 8, 752404. 10.3389/fmolb.2021.752404. [PubMed: 35004842]
41. Warburg O, Wind F, and Negelein E (1927). THE METABOLISM OF TUMORS IN THE BODY. J. Gen. Physiol. 8, 519–530. 10.1085/jgp.8.6.519. [PubMed: 19872213]
42. Wolf A, Agnihotri S, Micallef J, Mukherjee J, Sabha N, Cairns R, Hawkins C, and Guha A (2011). Hexokinase 2 is a key mediator of aerobic glycolysis and promotes tumor growth in human glioblastoma multiforme. J. Exp. Med. 208, 313–326. 10.1084/jem.20101470. [PubMed: 21242296]
43. Libby CJ, Gc S, Benavides GA, Fisher JL, Williford SE, Zhang S, Tran AN, Gordon ER, Jones AB, Tuy K, et al. (2021). A role for GLUT3 in glioblastoma cell invasion that is not recapitulated by GLUT1. Cell Adh. Migr. 15, 101–115. 10.1080/19336918.2021.1903684. [PubMed: 33843470]
44. Phillips E, Balss J, Bethke F, Pusch S, Christen S, Hielscher T, Schnölzer M, Fletcher MNC, Habel A, Tessmer C, et al. (2022). PFKFB4 interacts with FBXO28 to promote HIF-1a signaling in glioblastoma. Oncogenesis 11, 57. 10.1038/s41389-022-00433-3. [PubMed: 36115843]
45. Yang W, Zheng Y, Xia Y, Ji H, Chen X, Guo F, Lyssiotis CA, Aldape K, Cantley LC, and Lu Z (2012). ERK1/2-dependent phosphorylation and nuclear translocation of PKM2 promotes the Warburg effect. Nat. Cell Biol. 14, 1295–1304. 10.1038/ncb2629. [PubMed: 23178880]

46. Hu Y, Cao K, Wang F, Wu W, Mai W, Qiu L, Luo Y, Ge WP, Sun B, Shi L, et al. (2022). Dual roles of hexokinase 2 in shaping microglial function by gating glycolytic flux and mitochondrial activity. Nat. Metab. 4, 1756–1774. 10.1038/s42255-022-00707-5. [PubMed: 36536134]

47. DeWaal D, Nogueira V, Terry AR, Patra KC, Jeon SM, Guzman G, Au J, Long CP, Antoniewicz MR, and Hay N (2018). Hexokinase-2 depletion inhibits glycolysis and induces oxidative phosphorylation in hepatocellular carcinoma and sensitizes to metformin. Nat. Commun. 9, 446. 10.1038/s41467-017-02733-4. [PubMed: 29386513]

48. Freemerman AJ, Johnson AR, Sacks GN, Milner JJ, Kirk EL, Troester MA, Macintyre AN, Goraksha-Hicks P, Rathmell JC, and Makowski L (2014). Metabolic reprogramming of macrophages: glucose transporter 1 (GLUT1)-mediated glucose metabolism drives a proinflammatory phenotype. J. Biol. Chem. 289, 7884–7896. 10.1074/jbc.M113.522037. [PubMed: 24492615]

49. Ying H, Kimmelman AC, Lyssiotis CA, Hua S, Chu GC, Fletcher-Sananikone E, Locasale JW, Son J, Zhang H, Coloff JL, et al. (2012). Oncogenic Kras maintains pancreatic tumors through regulation of anabolic glucose metabolism. Cell 149, 656–670. 10.1016/j.cell.2012.01.058. [PubMed: 22541435]

50. Gopalbhai K, Jansen G, Beauregard G, Whiteway M, Dumas F, Wu C, and Meloche S (2003). Negative regulation of MAPKK by phosphorylation of a conserved serine residue equivalent to Ser212 of MEK1. J. Biol. Chem. 278, 8118–8125. 10.1074/jbc.M211870200. [PubMed: 12506122]

51. Li C, Liu DR, Li GG, Wang HH, Li XW, Zhang W, Wu YL, and Chen L (2015). CD97 promotes gastric cancer cell proliferation and invasion through exosome-mediated MAPK signaling pathway. World J. Gastroenterol. 21, 6215–6228. 10.3748/wjg.v21.i20.6215. [PubMed: 26034356]

52. Hilbig D, Sittig D, Hoffmann F, Rothemund S, Warmt E, Quaas M, Stürmer J, Seiler L, Liebscher I, Hoang NA, et al. (2018). Mechano-Dependent Phosphorylation of the PDZ-Binding Motif of CD97/ADGRE5 Modulates Cellular Detachment. Cell Rep. 24, 1986–1995. 10.1016/j.celrep.2018.07.071. [PubMed: 30134161]

53. Drube J, Haider RS, Matthees ESF, Reichel M, Zeiner J, Fritzwanker S, Ziegler C, Barz S, Klement L, Filor J, et al. (2022). GPCR kinase knockout cells reveal the impact of individual GRKs on arrestin binding and GPCR regulation. Nat. Commun. 13, 540. 10.1038/s41467-022-28152-8. [PubMed: 35087057]

54. McDonald PH, Chow CW, Miller WE, Laporte SA, Field ME, Lin FT, Davis RJ, and Lefkowitz RJ (2000). Beta-arrestin 2: a receptor-regulated MAPK scaffold for the activation of JNK3. Science 290, 1574–1577. 10.1126/science.290.5496.1574. [PubMed: 11090355]

55. Laporte SA, Oakley RH, Zhang J, Holt JA, Ferguson SS, Caron MG, and Barak LS (1999). The beta2-adrenergic receptor/betaarrestin complex recruits the clathrin adaptor AP-2 during endocytosis. Proc. Natl. Acad. Sci. USA 96, 3712–3717. 10.1073/pnas.96.7.3712. [PubMed: 10097102]

56. Eichler W, Hamann J, and Aust G (1997). Expression characteristics of the human CD97 antigen. Tissue Antigens 50, 429–438. 10.1111/j.1399-0039.1997.tb02897.x. [PubMed: 9389316]

57. Miwa T, Sun X, Ohta R, Okada N, Harris CL, Morgan BP, and Song WC (2001). Characterization of glycosylphosphatidylinositol-anchored decay accelerating factor (GPI-DAF) and transmembrane DAF gene expression in wild-type and GPI-DAF gene knockout mice using polyclonal and monoclonal antibodies with dual or single specificity. Immunology 104, 207–214. 10.1046/j.1365-2567.2001.01280.x. [PubMed: 11683961]

58. Haeryfar SMM, and Hoskin DW (2004). Thy-1: more than a mouse pan-T cell marker. J. Immunol. 173, 3581–3588. 10.4049/jimmunol.173.6.3581. [PubMed: 15356100]

59. Wandel E, Saalbach A, Sittig D, Gebhardt C, and Aust G (2012). Thy-1 (CD90) is an interacting partner for CD97 on activated endothelial cells. J. Immunol. 188, 1442–1450. 10.4049/jimmunol.1003944. [PubMed: 22210915]

60. Niu M, Xu S, Yang J, Yao D, Li N, Yan J, Zhong G, and Song G (2021). Structural basis for CD97 recognition of the decay-accelerating factor CD55 suggests mechanosensitive activation of adhesion GPCRs. J. Biol. Chem. 296, 100776. 10.1016/j.jbc.2021.100776. [PubMed: 33992645]

61. Doronina SO, Toki BE, Torgov MY, Mendelsohn BA, Cerveny CG, Chace DF, DeBlanc RL, Gearing RP, Bovee TD, Siegall CB, et al. (2003). Development of potent monoclonal antibody

auristatin conjugates for cancer therapy. Nat. Biotechnol. 21, 778–784. 10.1038/nbt832. [PubMed: 12778055]

62. Frenster JD, Inocencio JF, Xu Z, Dhaliwal J, Alghamdi A, Zagzag D, Bayin NS, and Placantonakis DG (2017). GPR133 Promotes Glioblastoma Growth in Hypoxia. Neurosurgery 64, 177–181. 10.1093/neuros/nyx227. [PubMed: 28899043]
63. Razpotnik R, Novak N, Čurin Šerbec V, and Rajcevic U (2017). Targeting Malignant Brain Tumors with Antibodies. Front. Immunol. 8, 1181. 10.3389/fimmu.2017.01181. [PubMed: 28993773]
64. Liang X, Wang Z, Dai Z, Zhang H, Zhang J, Luo P, Liu Z, Liu Z, Yang K, Cheng Q, and Zhang M (2023). Glioblastoma glycolytic signature predicts unfavorable prognosis, immunological heterogeneity, and ENO1 promotes microglia M2 polarization and cancer cell malignancy. Cancer Gene Ther. 30, 481–496. 10.1038/s41417-022-00569-9. [PubMed: 36494582]
65. Lunt SY, and Vander Heiden MG (2011). Aerobic glycolysis: meeting the metabolic requirements of cell proliferation. Annu. Rev. Cell Dev. Biol. 27, 441–464. 10.1146/annurev-cellbio-092910-154237. [PubMed: 21985671]
66. Lavoie H, Gagnon J, and Therrien M (2020). ERK signalling: a master regulator of cell behaviour, life and fate. Nat. Rev. Mol. Cell Biol. 21, 607–632. 10.1038/s41580-020-0255-7. [PubMed: 32576977]
67. Bando H, Atsumi T, Nishio T, Niwa H, Mishima S, Shimizu C, Yoshioka N, Bucala R, and Koike T (2005). Phosphorylation of the 6-phosphofructo-2-kinase/fructose 2,6-bisphosphatase/PFKFB3 family of glycolytic regulators in human cancer. Clin. Cancer Res. 11, 5784–5792. 10.1158/1078-0432.Ccr-05-0149. [PubMed: 16115917]
68. Houles T, Gravel SP, Lavoie G, Shin S, Savall M, Méant A, Grondin B, Gaboury L, Yoon SO, St-Pierre J, and Roux PP (2018). RSK Regulates PFK-2 Activity to Promote Metabolic Rewiring in Melanoma. Cancer Res. 78, 2191–2204. 10.1158/0008-5472.Can-17-2215. [PubMed: 29440170]
69. Hall A, Meyle KD, Lange MK, Klima M, Sanderhoff M, Dahl C, Abildgaard C, Thorup K, Moghimi SM, Jensen PB, et al. (2013). Dysfunctional oxidative phosphorylation makes malignant melanoma cells addicted to glycolysis driven by the (V600E)BRAF oncogene. Oncotarget 4, 584–599. 10.18632/oncotarget.965. [PubMed: 23603840]
70. Soto-Heredero G, Gómez de Las Heras MM., Gabandé-Rodríguez E., Oller J., and Mittelbrunn M. (2020). Glycolysis - a key player in the inflammatory response. FEBS J. 287, 3350–3369. 10.1111/febs.15327. [PubMed: 32255251]
71. Baillet A, Hograindleur MA, El Benna J, Grichine A, Berthier S, Morel F, and Paclet MH (2017). Unexpected function of the phagocyte NADPH oxidase in supporting hyperglycolysis in stimulated neutrophils: key role of 6-phosphofructo-2-kinase. Faseb j 31, 663–673. 10.1096/fj.201600720R. [PubMed: 27799347]
72. Yu Q, Wang Y, Dong L, He Y, Liu R, Yang Q, Cao Y, Wang Y, Jia A, Bi Y, and Liu G (2020). Regulations of Glycolytic Activities on Macrophages Functions in Tumor and Infectious Inflammation. Front. Cell. Infect. Microbiol. 10, 287. 10.3389/fcimb.2020.00287. [PubMed: 32596169]
73. Chang CH, Curtis JD, Maggi LB Jr., Faubert B, Villarino AV, O'Sullivan D, Huang SCC, van der Windt GJW, Blagih J, Qiu J, et al. (2013). Posttranscriptional control of T cell effector function by aerobic glycolysis. Cell 153, 1239–1251. 10.1016/j.cell.2013.05.016. [PubMed: 23746840]
74. Capasso M, Durrant LG, Stacey M, Gordon S, Ramage J, and Spendlove I (2006). Costimulation via CD55 on human CD4+ T cells mediated by CD97. J. Immunol. 177, 1070–1077. 10.4049/jimmunol.177.2.1070. [PubMed: 16818763]
75. Kishore M, Cheung KCP, Fu H, Bonacina F, Wang G, Coe D, Ward EJ, Colamatteo A, Jangani M, Baragetti A, et al. (2017). Regulatory T Cell Migration Is Dependent on Glucokinase-Mediated Glycolysis. Immunity 47, 875–889.e10. 10.1016/j.immuni.2017.10.017. [PubMed: 29166588]
76. Guak H, Al Habyan S, Ma EH, Aldossary H, Al-Masri M, Won SY, Ying T, Fixman ED, Jones RG, McCaffrey LM, and Krawczyk CM (2018). Glycolytic metabolism is essential for CCR7 oligomerization and dendritic cell migration. Nat. Commun. 9, 2463. 10.1038/s41467-018-04804-6. [PubMed: 29941886]

77. Wu D, Harrison DL, Szasz T, Yeh CF, Shentu TP, Meliton A, Huang RT, Zhou Z, Mutlu GM, Huang J, and Fang Y (2021). Single-cell metabolic imaging reveals a SLC2A3-dependent glycolytic burst in motile endothelial cells. Nat. Metab. 3, 714–727. 10.1038/s42255-021-00390-y. [PubMed: 34031595]

78. Shiraishi T, Verdone JE, Huang J, Kahlert UD, Hernandez JR, Torga G, Zarif JC, Epstein T, Gatenby R, McCartney A, et al. (2015). Glycolysis is the primary bioenergetic pathway for cell motility and cytoskeletal remodeling in human prostate and breast cancer cells. Oncotarget 6, 130–143. 10.18632/oncotarget.2766. [PubMed: 25426557]

79. Eichler W, Lohrenz A, Simon KU, Krohn S, Lange J, Bürger S, and Liebscher I (2019). The role of ADGRE5/CD97 in human retinal pigment epithelial cell growth and survival. Ann. N. Y. Acad. Sci. 1456, 64–79. 10.1111/nyas.14210. [PubMed: 31397926]

80. Yin Y, Xu X, Tang J, Zhang W, Zhangyuan G, Ji J, Deng L, Lu S, Zhuo H, and Sun B (2018). CD97 Promotes Tumor Aggressiveness Through the Traditional G Protein-Coupled Receptor-Mediated Signaling in Hepatocellular Carcinoma. Hepatology 68, 1865–1878. 10.1002/hep.30068. [PubMed: 29704239]

81. Sauzay C, Voutetakis K, Chatziioannou A, Chevet E, and Avril T (2019). CD90/Thy-1, a Cancer-Associated Cell Surface Signaling Molecule. Front. Cell Dev. Biol. 7, 66. 10.3389/fcell.2019.00066. [PubMed: 31080802]

82. Avril T, Etcheverry A, Pineau R, Obacz J, Jegou G, Jouan F, Le Reste PJ, Hatami M, Colen RR, Carlson BL, et al. (2017). CD90 Expression Controls Migration and Predicts Dasatinib Response in Glioblastoma. Clin. Cancer Res. 23, 7360–7374. 10.1158/1078-0432.Ccr-17-1549. [PubMed: 28939749]

83. Leyton L, Dáz J, Martínez S, Palacios E, Pérez LA, and Pérez RD (2019). Thy-1/CD90 a Bidirectional and Lateral Signaling Scaffold. Front. Cell Dev. Biol. 7, 132. 10.3389/fcell.2019.00132. [PubMed: 31428610]

84. Chesnelong C, Chaumeil MM, Blough MD, Al-Najjar M, Stechishin OD, Chan JA, Pieper RO, Ronen SM, Weiss S, Luchman HA, and Cairncross JG (2014). Lactate dehydrogenase A silencing in IDH mutant gliomas. Neuro Oncol. 16, 686–695. 10.1093/neuonc/not243. [PubMed: 24366912]

85. Grassian AR, Parker SJ, Davidson SM, Divakaruni AS, Green CR, Zhang X, Slocum KL, Pu M, Lin F, Vickers C, et al. (2014). IDH1 mutations alter citric acid cycle metabolism and increase dependence on oxidative mitochondrial metabolism. Cancer Res. 74, 3317–3331. 10.1158/0008-5472.Can-14-0772-t. [PubMed: 24755473]

86. Barger CJ, Branick C, Chee L, and Karpf AR (2019). Pan-Cancer Analyses Reveal Genomic Features of FOXM1 Overexpression in Cancer. Cancers 11, 251. 10.3390/cancers11020251. [PubMed: 30795624]

87. Morgenstern JP, and Land H (1990). Advanced mammalian gene transfer: high titre retroviral vectors with multiple drug selection markers and a complementary helper-free packaging cell line. Nucleic Acids Res. 18, 3587–3596. 10.1093/nar/18.12.3587. [PubMed: 2194165]

88. Campeau E, Ruhl VE, Rodier F, Smith CL, Rahmberg BL, Fuss JO, Campisi J, Yaswen P, Cooper PK, and Kaufman PD (2009). A versatile viral system for expression and depletion of proteins in mammalian cells. PLoS One 4, e6529. 10.1371/journal.pone.0006529. [PubMed: 19657394]

89. Frenster JD, and Placantonakis DG (2018). Establishing Primary Human Glioblastoma Tumorsphere Cultures from Operative Specimens. Methods Mol. Biol. 1741, 63–69. 10.1007/978-1-4939-7659-1_4. [PubMed: 29392690]

90. Xu Z, Kader M, Sen R, and Placantonakis DG (2018). Orthotopic Patient-Derived Glioblastoma Xenografts in Mice. Methods Mol. Biol. 1741, 183–190. 10.1007/978-1-4939-7659-1_14. [PubMed: 29392700]

91. Frenster JD, Inocencio J, and Placantonakis DG (2018). Lentiviral Transduction of Primary Human Glioblastoma Cultures. Methods Mol. Biol. 1741, 81–89. 10.1007/978-1-4939-7659-1_6. [PubMed: 29392692]

92. Frenster JD, and Placantonakis DG (2018). Bioluminescent In Vivo Imaging of Orthotopic Glioblastoma Xenografts in Mice. Methods Mol. Biol. 1741, 191–198. 10.1007/978-1-4939-7659-1_15. [PubMed: 29392701]

93. Jones DR, Wu Z, Chauhan D, Anderson KC, and Peng J (2014). A nano ultra-performance liquid chromatography-high resolution mass spectrometry approach for global metabolomic profiling and case study on drug-resistant multiple myeloma. Anal. Chem. 86, 3667–3675. 10.1021/ac500476a. [PubMed: 24611431]

94. Chen WW, Freinkman E, Wang T, Birsoy K, and Sabatini DM (2016). Absolute Quantification of Matrix Metabolites Reveals the Dynamics of Mitochondrial Metabolism. Cell 166, 1324–1337.e11. 10.1016/j.cell.2016.07.040. [PubMed: 27565352]

95. Simón-Manso Y, Lowenthal MS, Kilpatrick LE, Sampson ML, Telu KH, Rudnick PA, Mallard WG, Bearden DW, Schock TB, Tchekhovskoi DV, et al. (2013). Metabolite profiling of a NIST Standard Reference Material for human plasma (SRM 1950): GC-MS, LC-MS, NMR, and clinical laboratory analyses, libraries, and web-based resources. Anal. Chem. 85, 11725–11731. 10.1021/ac402503m. [PubMed: 24147600]

96. Smith CA, O'Maille G, Want EJ, Qin C, Trauger SA, Brandon TR, Custodio DE, Abagyan R, and Siuzdak G (2005). METLIN: a metabolite mass spectral database. Ther. Drug Monit. 27, 747–751. 10.1097/01.ftd.0000179845.53213.39. [PubMed: 16404815]

97. Jones E, Oliphant T, and Peterson P (2001). SciPy: Open Source Scientific Tools for Python.

98. Fellouse FA, Esaki K, Birtalan S, Raptis D, Cancasci VJ, Koide A, Jhurani P, Vasser M, Wiesmann C, Kossiakoff AA, et al. (2007). High-throughput generation of synthetic antibodies from highly functional minimalist phage-displayed libraries. J. Mol. Biol. 373, 924–940. 10.1016/j.jmb.2007.08.005. [PubMed: 17825836]

99. Paduch M, Koide A, Uysal S, Rizk SS, Koide S, and Kossiakoff AA (2013). Generating conformation-specific synthetic antibodies to trap proteins in selected functional states. Methods 60, 3–14. 10.1016/j.ymeth.2012.12.010. [PubMed: 23280336]

100. Miller KR, Koide A, Leung B, Fitzsimmons J, Yoder B, Yuan H, Jay M, Sidhu SS, Koide S, and Collins EJ (2012). T cell receptor-like recognition of tumor in vivo by synthetic antibody fragment. PLoS One 7, e43746. 10.1371/journal.pone.0043746. [PubMed: 22916301]

101. Oury J, Zhang W, Leloup N, Koide A, Corrado AD, Ketavarapu G, Hattori T, Koide S, and Burden SJ (2021). Mechanism of disease and therapeutic rescue of Dok7 congenital myasthenia. Nature 595, 404–408. 10.1038/s41586-021-03672-3. [PubMed: 34163073]

102. Lo M, Kim HS, Tong RK, Bainbridge TW, Vernes JM, Zhang Y, Lin YL, Chung S, Dennis MS, Zuchero YJY, et al. (2017). Effector-attenuating Substitutions That Maintain Antibody Stability and Reduce Toxicity in Mice. J. Biol. Chem. 292, 3900–3908. 10.1074/jbc.M116.767749. [PubMed: 28077575]

103. Doronina SO, Mendelsohn BA, Bovee TD, Cerveny CG, Alley SC, Meyer DL, Oflazoglu E, Toki BE, Sanderson RJ, Zabinski RF, et al. (2006). Enhanced activity of monomethylauristatin F through monoclonal antibody delivery: effects of linker technology on efficacy and toxicity. Bioconjug. Chem. 17, 114–124. 10.1021/bc0502917. [PubMed: 16417259]

## Highlights

- CD97 is an adhesion GPCR that is *de novo* expressed in GBM compared to healthy brain
- CD97 promotes tumorigenesis and glycolytic metabolism in GBM via MAPK signaling
- Phosphorylation of the C terminus of CD97 leads to β-arrestin recruitment
- GBM cells can be selectively killed using a CD97-targeting antibody-drug conjugate

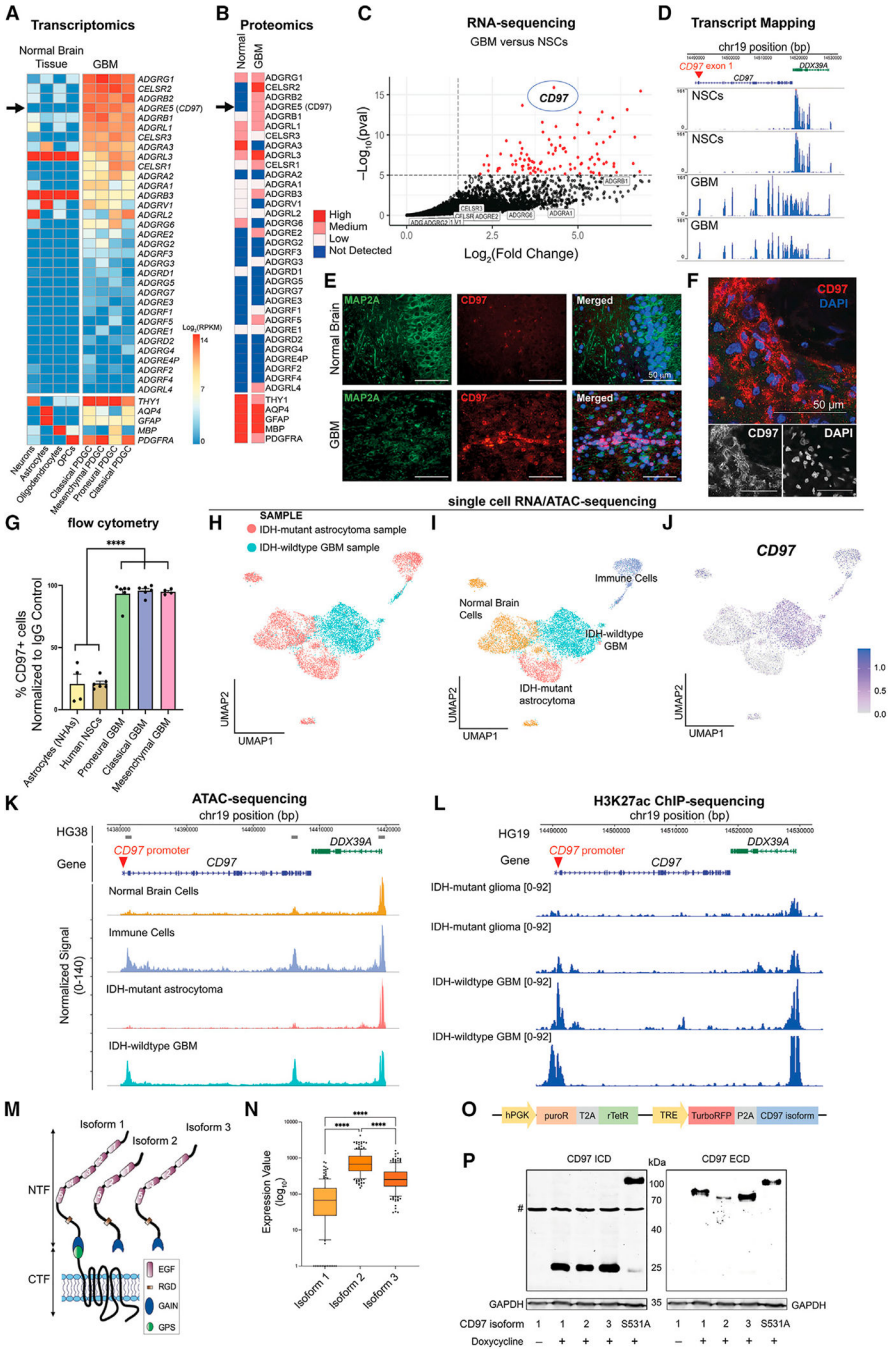


**Figure 1. CD97 (ADGRE5) is *de novo* expressed in GBM.**

(A) Heatmap showing $\log_2$ expression of transcripts encoding aGPCRs and known markers in healthy brain tissue and GBM ($\log_2$(RPKM)). *CD97* (*ADGRE5*) is indicated by an arrow.

(B) Heatmap showing protein expression of aGPCRs and known markers in healthy brain tissue and GBM. CD97 (ADGRE5) is indicated by an arrow.[34]

(C) Volcano plot showing upregulated genes in a PDGC compared to human NSCs. All aGPCRs are labeled. *CD97* (circled) was significantly upregulated (adjusted p value [$p_{adj}$] < 0.00001, $\log_2$(fold change) > 1.5).

(D) Transcripts from bulk RNA-seq data collected from two PDGC replicates and two NSC replicates were aligned along the *CD97* locus. The red arrowhead signifies the first *CD97* exon.
(E) Immunofluorescent and Hoechst 33342-stained specimen of human temporal lobe (healthy) and GBM. MAP2A is a neuronal marker.
(F) Confocal microscopy images of a GBM specimen stained with an antibody against the CD97 extracellular domain (ECD) (red) and DAPI (blue). A merged color image is accompanied by black and white single-channel images.
(G) CD97 surface staining via flow cytometry using an allophycocyanin (APC)-conjugated antibody in proneural (n = 6), classical (n = 6), and mesenchymal (n = 4) PDGCs, NSCs (n = 6), and NHAs (n = 4) (unpaired t test; ****$p < 0.0001$).
(H) Single-cell RNA/ATAC-seq data from IDH-mutant astrocytoma and IDH-WT GBM surgical specimens. Single cells are color-coded based on their tumor of origin.
(I) Cluster identities were characterized and named based on their corresponding gene expression profiles. Single cells are colored based on broad cluster identities.
(J) *CD97* expression in cell clusters based on integrated data.
(K) ATAC peaks associated with the *CD97* locus were extracted from single-cell ATAC-seq and integrated based on the clusters in (I). The red arrowhead signifies the *CD97* promoter. Also shown are peaks corresponding to the *DDX39A* promoter, which is expressed in all cell clusters.
(L) H3K27ac ChIP-seq from the GEO shows peaks associated with the *CD97* locus for IDH-WT GBM and IDH-mutant anaplastic astrocytoma. The red arrowhead signifies the *CD97* promoter.
(M) Schematic representation of the structure of three CD97 splice isoforms. EGF, epidermal growth factor-like repeat; RGD, arginylglycylaspartic acid domain; GAIN, GPCR autoproteolysis-inducing domain; GPS, GPCR proteolysis site; NTF, N-terminal fragment; CTF, C-terminal fragment. Note that for isoforms 2 and 3, only the NTF is shown.
(N) Bulk RNA-seq data from the GBM dataset of TCGA Splice Variant Database (TSVdb) were used to quantify CD97 isoform expression. Orange boxes are centered around the median and encompass the two middle quartiles (n = 166 per isoform; ANOVA $F_{2,330} = 283.3$, $p < 0.0001$; Tukey's multiple comparisons test: isoform 1 vs. isoform 2: ****$p < 0.0001$; isoform 1 vs. isoform 3: ****$p < 0.0001$; isoform 2 vs. isoform 3: ****$p < 0.0001$).
(O) Schematic representation of the tet-inducible vector used for CD97 isoform overexpression.
(P) Immunoblots for the CD97 intracellular domain (ICD, equivalent to the CTF) and the ECD (equivalent to NTF). CD97 S531A is an uncleavable point mutant of isoform 1. Non-specific bands are indicated by a hash symbol (#). The same membrane was stained for CD97 ICD and then stripped for CD97 ECD staining.
Error bars indicate SEM.

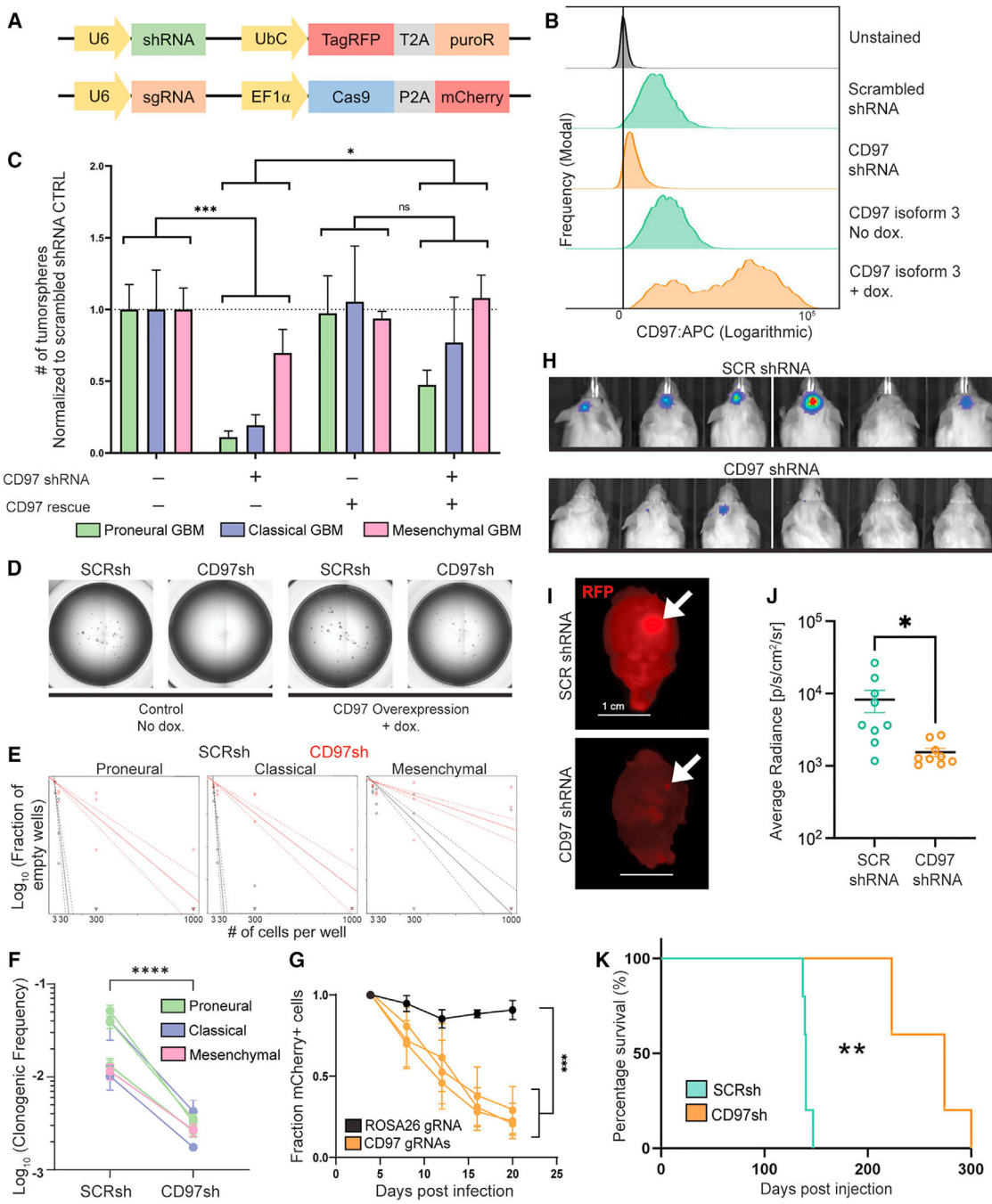


**Figure 2. CD97 is essential for tumor initiation *in vitro* and *in vivo*.**

(A) Schematic representations of the shRNA and CRISPR constructs used to knock down and knock out CD97, respectively.

(B) Histograms of CD97 surface staining following knockdown or overexpression of isoform 3 of CD97 in a PDGC.

(C) Bar graph visualizing tumorsphere formation following knockdown of CD97 and followed by rescue with a dox-inducible and a shRNA-resistant form of CD97 isoform 3 (n = 5 for each PDGC; two-way ANOVA $F_{3,36} = 9.795$, $p < 0.0001$; Tukey's multiple

comparisons test: empty vector (EV) SCRsh vs. EV CD97sh: ***$p < 0.001$; EV CD97sh vs. overexpressed (OE) CD97sh: *$p < 0.01$; OE SCRsh vs. OE CD97sh: ns, $p > 0.05$).

(D) Representative wells from the tumorsphere formation assay quantified in (C) before and after dox-induced rescue.

(E) ELDA plots for three PDGCs are displayed.

(F) Summary plot showing calculated clonogenic frequencies for all tested PDGCs after CD97 knockdown based on ELDA assays. Paired samples are connected with a line (n = 3 per PDGC; two-way ANOVA $F_{1,28} = 75.24$, $p < 0.0001$).

(G) Graph showing compromised viability of PDGCs infected with three separate gRNAs against CD97 (orange) compared to a control gRNA against the human homolog of *ROSA26* (black) in a cell competition assay (n = 3 per gRNA; two-way ANOVA $F_{4,40} = 10.37$, $p < 0.001$; Tukey's multiple comparisons test: ROSA26 vs. CD97: days 4, 8, and 12: ns, $p > 0.05$; days 16 and 20: ***$p < 0.001$).

(H) Bioluminescent images taken with IVIS of intracranial GBM xenografts 90 days after injection.

(I) Immunofluorescent images of mouse brains injected with PDGCs lentivirally infected with the indicated shRNA construct, the TagRFP fluorophore, and luciferase. White arrows indicate the resulting tumor at the site of injection.

(J) Graph depicting the average bioluminescent radiance captured by IVIS for mice harboring PDGC xenografts (n = 9 mice per group; unpaired t test; *$p < 0.05$).

(K) Kaplan-Meier survival curve showing significantly increased survival of mice xenografted with a PDGC harboring CD97 shRNA (n = 5 mice per group; log-rank test; **$p < 0.01$).

Error bars indicate SEM.

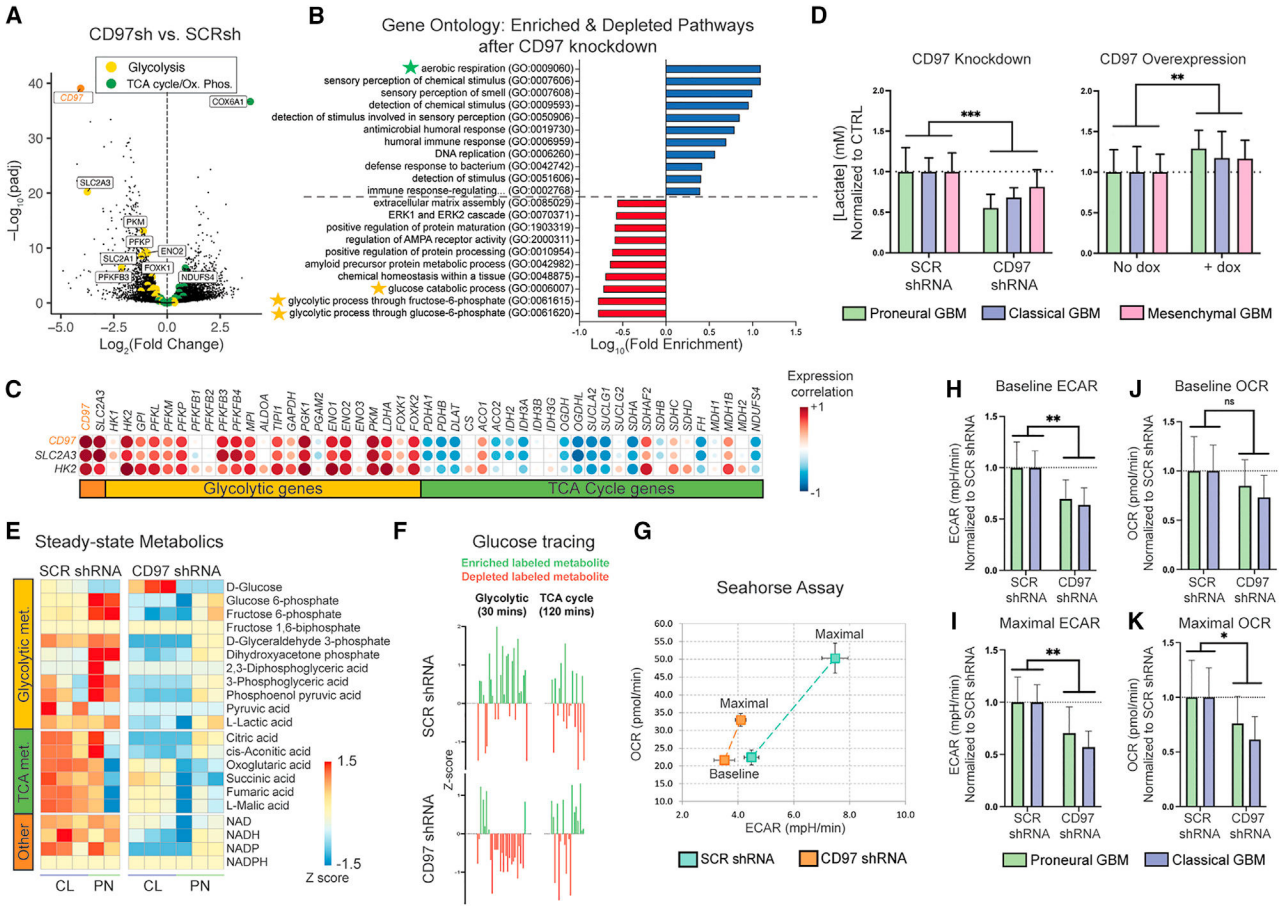


**Figure 3. CD97 knockdown impairs glycolytic metabolism in GBM.**

(A) Volcano plot derived from bulk RNA-seq data collected from PDGCs lentivirally infected with the SCR or CD97 shRNA (n = 3 biological replicates for each). Genes involved in canonical glycolysis and glucose transport are represented as large yellow points. Genes involved in the TCA cycle and OXPHOS (cytochrome oxidase subunits) are represented as large green points. *CD97* is represented by an orange point.

(B) The top ten enriched and depleted pathways determined by the largest fold enrichment among downregulated genes using GO PANTHER pathway enrichment analysis. Stars indicate metabolic pathways.

(C) Correlation matrix from bulk RNA-seq data collected from PDGCs following knockdown or overexpression of CD97 shows high correlation between *CD97* and glycolysis-related genes and anti-correlation with TCA cycle-related genes. *HK2* (hexokinase 2) and *SLC2A3* (glucose transporter 3 [GLUT3]) transcripts are both included because they have been implicated in Warburg metabolism.

(D) Bar graph showing decreased lactate production after knockdown of CD97 (n = 6 per PDGC; two-way ANOVA $F_{1,15} = 27.24$, $p < 0.001$) and increased lactate production after CD97 overexpression in PDGCs (n = 3 per PDGC; two-way ANOVA $F_{1,6} = 26.07$, $p < 0.01$).

(E) Steady-state metabolomic data reveal depletion of glycolytic metabolites after knockdown of CD97 in PDGCs (PN [proneural], n = 2–3 [one replicate was removed for technical reasons]; CL [classical], n = 3).

(F) Depleted (red) and enriched (green) heavy-labeled glycolytic and TCA cycle metabolites after a heavy-labeled glucose tracing experiment.

(G) Representative Seahorse Cell Energy Phenotype graph showing OCR and ECAR changes before (baseline) and after (maximal) addition of mitochondrial stressors.

(H and I) Bar graphs quantifying baseline and maximal ECAR (n = 6 per PDGC; baseline: two-way ANOVA $F_{1,10} = 14.06$; **$p < 0.01$; maximal: two-way ANOVA $F_{1,10} = 17.87$, $p < 0.01$).

(J and K) Bar graphs quantifying baseline and maximal OCR (n = 6 per PDGC; baseline: two-way ANOVA $F_{1,10} = 2.820$, $p > 0.05$; maximal: two-way ANOVA $F_{1,10} = 5.474$; *$p < 0.05$).

Error bars indicate SEM.

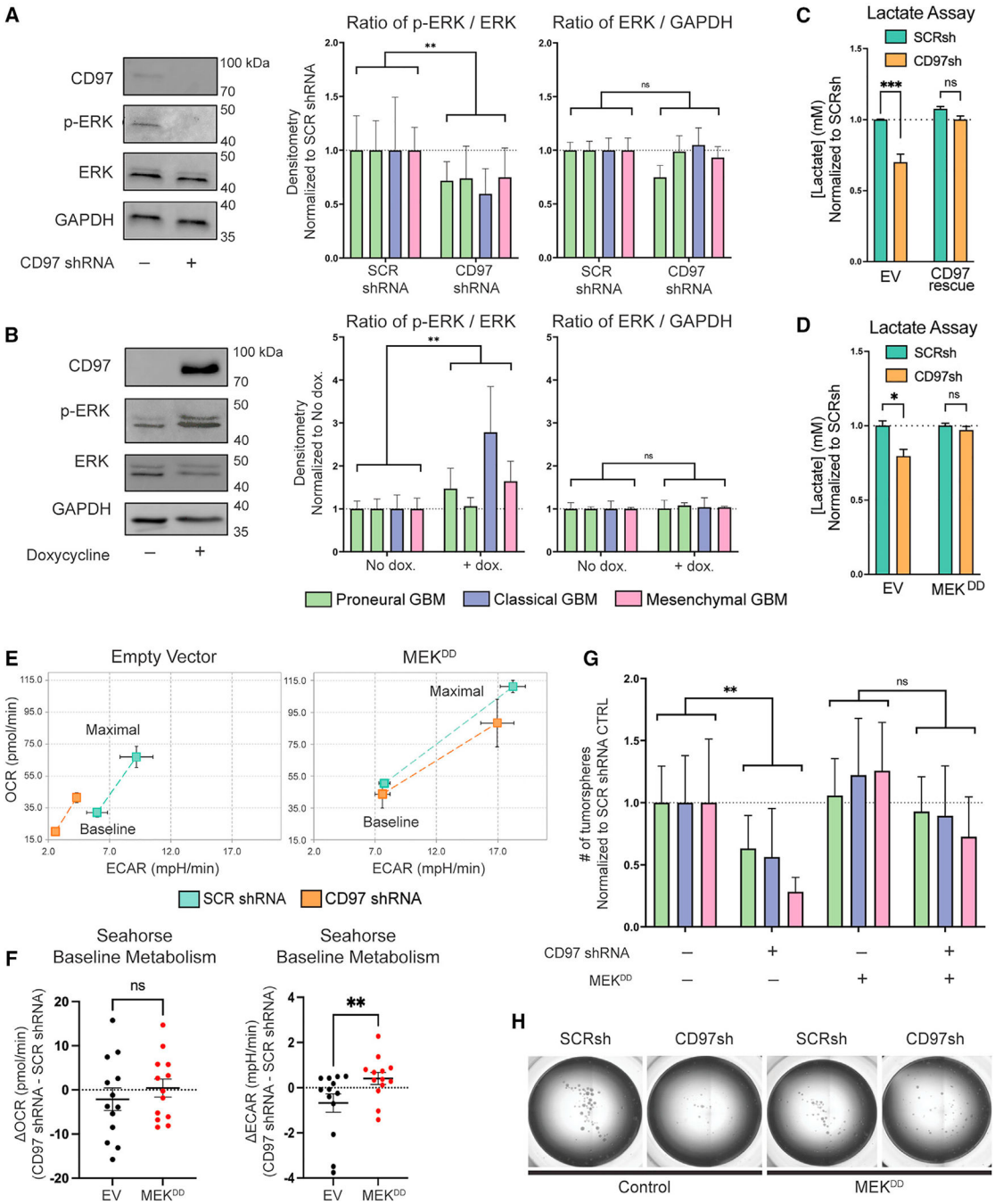


**Figure 4. CD97 activates the MAPK signaling pathway to regulate glycolysis and tumorsphere formation.**

(A) Immunoblot for phosphorylated ERK1/ERK2, total ERK1/ERK2, and GAPDH in PDGCs following CD97 knockdown. Red pixels indicate saturation. Quantification of densitometry ratios is also shown (phosphorylated [p]-ERK/ERK: n = 5–6 per PDGC; two-way ANOVA $F_{1,17} = 8.407$, $p < 0.01$; ERK/GAPDH: n = 5–6 per PDGC; two-way ANOVA $F_{1,17} = 2.796$, $p > 0.05$).

(B) Immunoblot for p-ERK1/ERK2, total ERK1/ERK2, and GAPDH in a PDGC following dox-induced overexpression of CD97. Quantification of densitometry ratios is also shown

(all isoforms compiled for each PDGC) (p-ERK/ERK: n = 4–8 per PDGC; two-way ANOVA $F_{1,21} = 10.98$, $p < 0.01$; ERK/GAPDH: n = 4–8; two-way ANOVA $F_{1,21} = 1.554$, $p > 0.05$).

(C) Bar graph showing that CD97 overexpression rescues lactate levels after CD97 knockdown (n = 3–6; ANOVA $F_{3,15} = 25.75$, $p < 0.0001$; Tukey's multiple comparisons test: EV SCRsh vs. EV CD97sh: ***$p < 0.001$; CD97 rescue SCRsh vs. CD97 rescue CD97sh: ns $p > 0.05$).

(D) Bar graph showing restored lactate levels upon rescue with the $MEK^{DD}$ mutant (n = 3–8; ANOVA $F_{3,19} = 8.216$, $p < 0.01$; Tukey's multiple comparisons test: EV SCRsh vs. EV CD97sh: *$p < 0.05$; $MEK^{DD}$ SCRsh vs. $MEK^{DD}$ CD97sh: ns $p > 0.05$).

(E) Seahorse Cell Energy Phenotype graphs showing OCR and ECAR changes before (baseline) and after (maximal) addition of mitochondrial stressors in knockdown cells after introduction of the $MEK^{DD}$ mutant or an EV control.

(F) Quantification of the difference in baseline OCR and ECAR between SCR and CD97 knockdown PDGCs after introduction of the $MEK^{DD}$ mutant or an EV control (n = 13 [all PDGCs compiled]; unpaired t test; ns $p > 0.05$; **$p < 0.01$).

(G) Bar graph visualizing tumorsphere formation following CD97 knockdown and introduction of the $MEK^{DD}$ mutant (n = 8–9 per PDGC; two-way ANOVA $F_{3,66} = 8.707$, $p < 0.0001$; Tukey's multiple comparisons test: EV SCRsh vs. EV CD97sh: **$p < 0.01$; $MEK^{DD}$ SCRsh vs. $MEK^{DD}$ CD97sh: ns $p > 0.05$).

(H) Representative wells from the assay in (G).

Error bars indicate SEM.

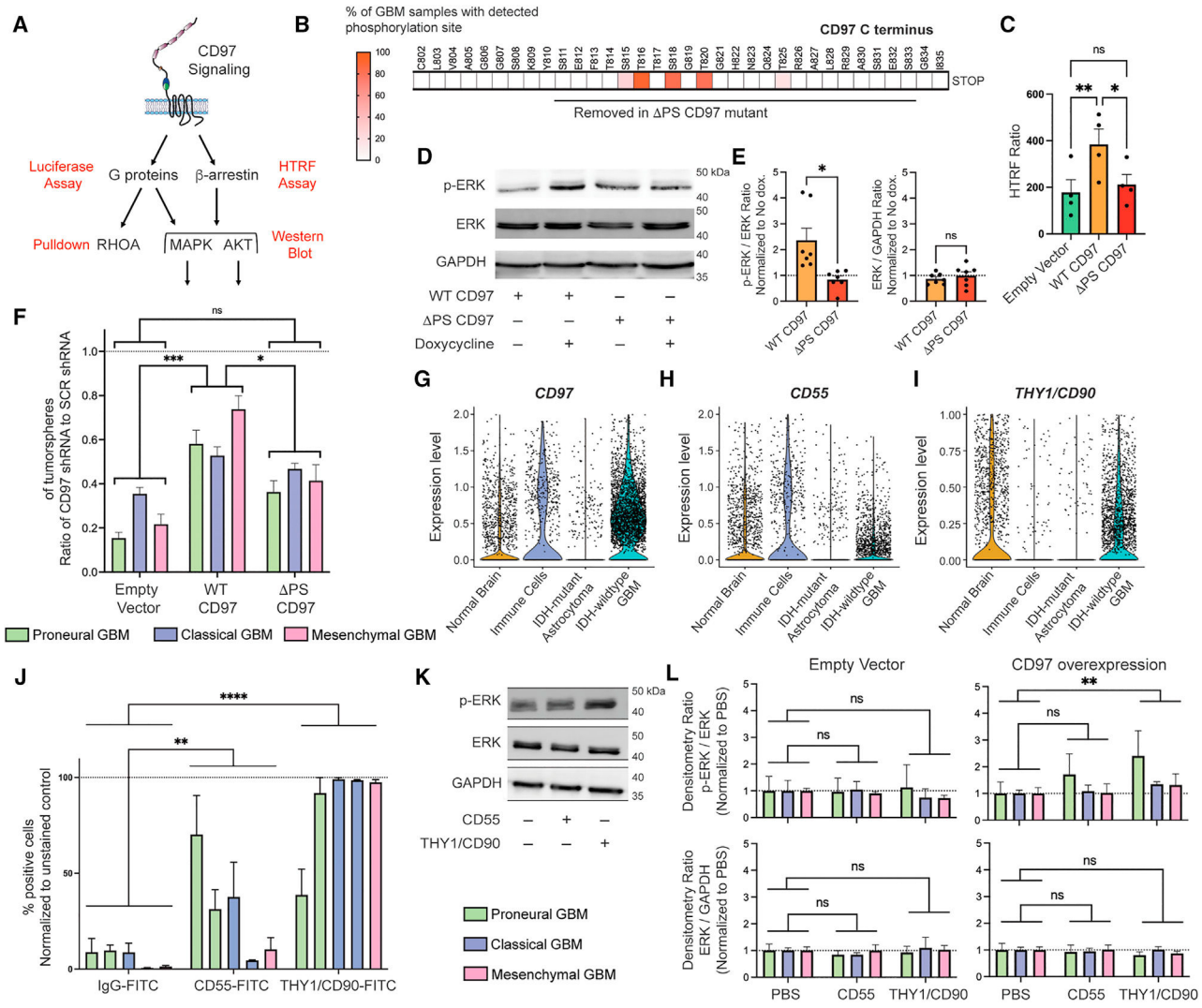


**Figure 5. CD97 activates the MAPK signaling cascade through recruitment of β-arrestin to its phosphorylated C terminus and by association with THY1/CD90.**

(A) Schematic of possible CD97 signaling mechanisms tested. Listed in red are the methods for testing.

(B) Phosphoproteomic data collected from GBM samples identify five phosphorylation sites on the CD97 cytosolic C terminus. The heatmap depicts the percentage of GBM samples with the detected phosphorylation site.

(C) Homogenous time-resolved fluorescence (HTRF) ratios from a β-arrestin recruitment assay performed after overexpression of WT CD97 or the ΔPS mutant. Two PDGCs (n = 2 for each) are compiled (n = 4 per condition; unpaired t test; ns $p > 0.05$; *$p < 0.05$; **$p < 0.01$).

(D) Immunoblot for p-ERK1/ERK2 after overexpression of WT CD97 or the ΔPS mutant.

(E) Bar graphs displaying densitometry ratios from (D) (n = 7; paired t test; ns $p > 0.05$; *$p < 0.05$). Two PDGCs (n = 3–4 for each) are compiled.

(F) Bar graphs depicting the number of tumorspheres in a tumorsphere formation assay after CD97 knockdown followed by overexpression of shRNA-resistant forms of WT CD97 or

the ΔPS mutant. The SCR shRNA groups used for normalization are not shown (n = 4 per PDGC; ANOVA $F_{5,12} = 80.79$, $p < 0.0001$; Tukey's multiple comparisons test: EV vs. WT: ***$p < 0.001$; EV vs. ΔPS: ns $p > 0.05$; WT vs. ΔPS: *$p < 0.05$).

(G–I) Single-cell RNA-/ATAC-seq data from Figure 1I showing expression of *CD97*, *CD55*, and *THY1/CD90*.

(J) A bar graph depicting the percentage of positive cells measured by flow cytometry after surface staining of PDGCs with fluorescein isothiocyanate (FITC)-conjugated antibodies against CD55, THY1/CD90, and an IgG control (n = 3 for each PDGC; two-way ANOVA $F_{2,20} = 95.11$, $p < 0.0001$; Tukey's multiple comparisons test: IgG vs. CD55: **$p < 0.01$; IgG vs. CD90: ****$p < 0.00001$; CD55 vs. CD90: ****$p < 0.01$).

(K) Immunoblot for p-ERK1/ERK2 from CD97-overexpressing PDGCs plated on laminin or recombinant forms of putative ligands CD55 and THY1/CD90.

(L) Quantification of densitometry ratios from immunoblots in (K) (n = 2–4 per PDGC; EV p-ERK/ERK: two-way ANOVA $F_{2,6} = 0.9450$, $p > 0.05$; EV ERK/GAPDH: two-way ANOVA $F_{2,6} = 1.047$, $p > 0.05$; CD97 overexpression p-ERK/ERK: two-way ANOVA $F_{2,16} = 12.48$, $p < 0.001$; Tukey's multiple comparisons test: laminin vs. CD55: ns, $p < 0.05$; laminin vs. CD90: ***$p < 0.001$; CD97 overexpression ERK/GAPDH: two-way ANOVA $F_{2,16} = 2.257$, ns $p > 0.05$).

Error bars indicate SEM.

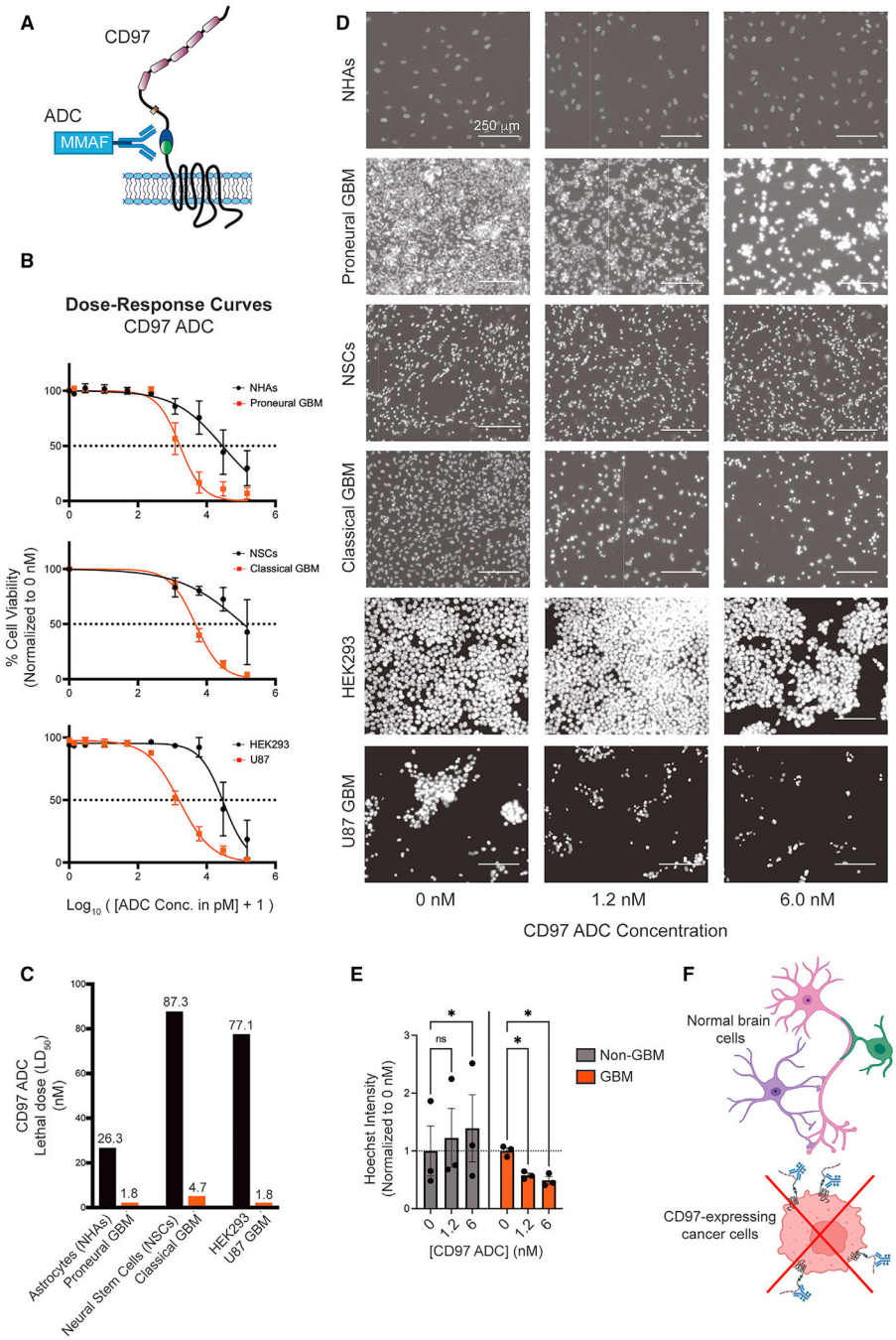


**Figure 6. A CD97-targeting antibody-drug conjugate demonstrates enhanced killing of PDGCs compared to NSCs and NHAs.**

(A) Schematic of the MMAF-conjugated ADC binding to the CD97 receptor.

(B) Dose-response curves generated from WST8 cell viability assays (n = 3 biological replicates based on technical triplicates) after treatment of PDGCs, U87 GBM cells, NHAs, NSCs, and HEK293 cells with the CD97 ADC.

(C) Bar graph displaying the $LD_{50}$ values (in nM) for the CD97 ADC on all six cell lines as calculated from dose-response curves in (B). Curves were based on a nonlinear regression fit.

(D) Representative images of Hoechst 33342-stained cells after 6 days of treatment with different concentrations of the CD97 ADC.
(E) Quantification of Hoechst intensity in Figure 5D. Values are normalized to the 0 nM condition. NHAs, NSCs, and HEK293 cells are compiled (non-GBM; black) and the three GBM lines are compiled (GBM; red) to make differences more evident (n = 1 for each cell line; two-way ANOVA $F_{2,8} = 12.13$, $p < 0.01$; Tukey's multiple comparisons test: non-GBM: 0 vs. 1.2 nM: ns $p > 0.05$; 0 vs. 6 nM: *$p < 0.05$; GBM: 0 vs. 1.2 nM: *$p < 0.05$; 0 vs. 6 nM: *$p < 0.05$).
(F) Diagram of the CD97 ADC killing CD97-expressing GBM cells and sparing healthy brain cells.
Error bars indicate SEM.

## KEY RESOURCES TABLE

| REAGENT or RESOURCE | SOURCE | IDENTIFIER |
|---|---|---|
| Antibodies | | |
| Rabbit monoclonal anti-CD97 antibody (N-terminal) | Abcam | AB108368; RRID:AB_10865208 |
| Rabbit polyclonal anti-CD97 antibody (C-terminal) | Abcam | AB155798; RRID:AB_2924416 |
| Mouse monoclonal CD97 Antibody APC-conjugated (MEM-180) | Thermo Fisher | MA5-16825; RRID:AB_2538307 |
| Mouse monoclonal anti-MAP2 antibody, clone AP20 | Sigma-Aldrich | M2320; RRID:AB_609904 |
| Goat polyclonal anti-IgG (human) antibody APC-conjugated | R&D | F0135; RRID: n/a |
| Mouse monoclonal anti-CD55 antibody FITC-conjugated | BD Biosciences | 555693; RRID:AB_396044 |
| Mouse monoclonal antibody anti-CD90 antibody FITC-conjugated | BD Biosciences | 555595; RRID:AB_395969 |
| Goat polyclonal anti-GAPDH | Invitrogen | PA1-9046; RRID:AB_1074703 |
| Secondary donkey anti-mouse Alexa Fluor plus 488 | Invitrogen | A32766; RRID:AB_2762823 |
| Secondary goat anti-rabbit Alexa Fluor plus 488 | Invitrogen | A32790; RRID:AB_2762833 |
| Secondary donkey anti-rabbit Alexa Fluor plus 555 | Invitrogen | A32794; RRID:AB_2762834 |
| Secondary donkey anti-mouse Alexa Fluor plus 555 | Invitrogen | A32773; RRID:AB_2762848 |
| Secondary donkey anti-goat Alexa Fluor plus 647 | Invitrogen | A32849; RRID:AB_2762840 |
| Secondary chicken anti-mouse HRP-conjugated | Invitrogen | A15975; RRID:AB_2534649 |
| Secondary chicken anti-rabbit HRP-conjugated | Invitrogen | A15987; RRID:AB_2534661 |
| Rabbit monoclonal p44/42 MAPK (Erk1/2)(137F5) antibody | Cell Signaling | 4695; RRID:AB_390779 |
| Rabbit monoclonal phosphor-p44/42 MAPK (Erk1/2) (Thr202/Tyr204) (D13.14.4E) antibody | Cell Signaling | 4370; RRID:AB_2315112 |
| Rabbit polyclonal anti-glucose transporter GLUT3 antibody (ab15311) | Abcam | AB15311; RRID:AB_301846 |
| Rabbit polyclonal Akt antibody | Cell Signaling | 9272S; RRID:AB_329827 |
| Rabbit polyclonal phospho-Akt (Ser473) antibody | Cell Signaling | 9271S; RRID:AB_329825 |
| Rabbit polyclonal anti-Ki67 antibody (ab15580) | Abcam | AB15580; RRID:AB_443209 |
| CD97-MMAF Antibody Drug Conjugate (ADC) | This paper | N/A |
| Chemicals, peptides, and recombinant proteins | | |
| EDTA (0.5 M), pH 8.0 | Thermo Fisher | AM9260G |
| DDM (n-dodecyl β-D-maltoside) (10%) | Thermo Fisher | BN2005 |
| Dulbecco's modified Eagle's medium (DMEM) | Gibco | 11965–118 |

| REAGENT or RESOURCE | SOURCE | IDENTIFIER |
|---|---|---|
| DMEM/F12 Medium | Thermo Fisher | 11330057 |
| Eagle's Minimum Essential Medium (EMEM) | ATCC | 30–2003 |
| Insulin | Sigma-Aldrich | I0516 |
| Glucose | Thermo Fisher | A2494001 |
| Sodium pyruvate | Gibco | 11360070 |
| Fetal bovine serum (FBS) | Peak Serum | PS-FB2 |
| Neurobasal Medium | Gibco | 21103049 |
| EGF | R&D | 236-EG-01M |
| bFGF | R&D | 233-FB-01M |
| GlutaMAX Supplement | Gibco | 35050061 |
| MEM Non-Essential Amino Acids | Gibco | 11140050 |
| N2 Supplement | Gibco | 17-502-049 |
| B27-Supplement | Gibco | 12587010 |
| Poly-L-Ornithine solution | Sigma | P4957-50mL |
| Laminin | Thermo Fisher | 23017015 |
| Lipofectamine 2000 | Invitrogen | 11668-019 |
| Trypsin | Thermo Fisher | 25300054 |
| Accutase | Innovative Cell Technologies | AT104 |
| Lenti-X Concentrator | Takara | 631231 |
| Thy1/CD90 Protein, Human, Recombinant | SinoBiological | 16897-HCCH |
| Recombinant Human CD55/DAF Protein | R&D | 2009-CD |
| D-glucose$^{13}C_6$ | Sigma-Aldrich | 389374 |
| Neurobasal-A medium, no D-glucose, no sodium pyruvate | Thermo Fisher | A2477501 |
| Glycine/Hydrazine 0.6M solution | Sigma-Aldrich | G5418 |
| 240mM NAD+ | Sigma-Aldrich | N0632 |
| Lactate dehydrogenase (5U/uL) | Roche | 10127230001 |
| Lactate | Thermo Fisher | AC18987-050 |
| G418-sulfate | Corning | 61-234-RG |
| Methanol | Thermo Fisher | 615130025 |
| Metabolomics amino acid mix standard | Cambridge Isotope Laboratories, Inc. | MSK-A2-1.2 |
| Disruption Beads | Research Products International | 9835 |
| LC/MS Grade Water | Fisher Scientific | W6500 |
| Critical commercial assays | | |
| HTRF-based b-arrestin2 recruitment kit | CisBio | 62BDBAR2PEB |
| Seahorse XF Cell Energy Phenotype Test Kit | Agilent | 103325–100 |
| RhoA Pull-down activation assay biochem kit | Cytoskeleton, Inc. | BK036 |

| REAGENT or RESOURCE | SOURCE | IDENTIFIER |
|---|---|---|
| Deposited Data | | |
| Bulk RNA-sequencting data | This paper | GEO: GSE230393 |
| Single cell multiomic data | This paper | GEO: GSE230389 |
| Experimental models: Cell lines | | |
| Lenti-X 293T cell Line | Takara | 632180 |
| Patient-derived GBM cultures | This paper | N/A |
| U-87 MG GBM cells | ATCC | HTB-14; RRID:CVCL_0022 |
| Normal Human Astrocytes | Lonza | CC-2565 |
| Human embryonic stem cells | WA09 | |
| GRK Knockout 293T cell Lines | Drube et al.[53] | ΔGRK2, ΔGRK6, ΔGRK2/6 |
| Oligonucleotides | | |
| caccGTCACAAGTCTCCGTCGGGG | Eurofins Genomics | CD97 gRNA1 For |
| aaacCCCCGACGGAGACTTGTGAC | Eurofins Genomics | CD97 gRNA1 Rev |
| caccGTTCATACCTGAGGATCCGA | Eurofins Genomics | CD97 gRNA2 For |
| aaacTCGGATCCTCAGGTATGAAC | Eurofins Genomics | CD97 gRNA2 Rev |
| caccgTCTGGAAGAGTGACAGCGAC | Eurofins Genomics | CD97 gRNA4 For |
| aaacGTCGCTGTCACTCTTCCAGAc | Eurofins Genomics | CD97 gRNA4 Rev |
| caccgGCTAGCCTCTTGTCGCCGAT | Eurofins Genomics | hRosa26 gRNA2 For |
| aaacATCGGCGACAAGAGGCTAGCc | Eurofins Genomics | hRosa26 gRNA2 Rev |
| accgCCGGGCGATCCTTATGGCTCATTATCTCGAGATAATGAGCCATAAGGATCGCTTTTT | Eurofins Genomics | CD97 shRNA For |
| cgaa AAAAA GCGATCCTTATGGCT CATTAT CTCGAG ATAATGAGCCAT AAGGATCGC CCGG | Eurofins Genomics | CD97 shRNA Rev |
| accgccggtcctaaggttaagtcgccctcctcgaggagggcgacttaaccttaggattttt | Eurofins Genomics | Scrambled shRNA For |
| cgaaaaaaatcctaaggttaagtcgccctcctcgaggagggcgacttaaccttaggaccgg | Eurofins Genomics | Scrambled shRNA Rev |
| Recombinant DNA | | |
| pRSI9-U6-(sh)-UbiC-TagRFP-2A-Puro | Chenchik & Frangou | Addgene 28289; RRID:Addgene_28289 |
| pRSI9-U6-(CD97sh)-UbiC-TagRFP-2A-Puro | Martin et al.[26] | N/A |
| pRSI9-U6-(SCRsh)-UbiC-TagRFP-2A-Puro | This paper | N/A |

| REAGENT or RESOURCE | SOURCE | IDENTIFIER |
|---|---|---|
| pCW57-RFP-P2A-MCS | Barger et al.[86] | Addgene 78933; RRID:Addgene_78933 |
| pBabe-neo | Morgenstern et al.[87] | Addgene 1767; RRID:Addgene_1767 |
| pLenti PGK Blast V5-Luc | Campeau et al.[88] | Addgene 19166; RRID:Addgene_19166 |
| LentiCRISPRv2-mCherry | Smogorzewska | Addgene 99154; RRID:Addgene_99154 |
| pCW57-RFP-P2A-CD97 isoform 1 | This paper | N/A |
| pCW57-RFP-P2A-CD97 isoform 2 | This paper | N/A |
| pCW57-RFP-P2A-CD97 isoform 3 | This paper | N/A |
| pCW57-RFP-P2A-CD97 S531A | This paper | N/A |
| pCW57-RFP-P2A-CD97 DPS | This paper | N/A |